



Black Hole–Galaxy Scaling Relationships for Active Galactic Nuclei with Reverberation Masses

Misty C. Bentz  and Emily Manne-Nicholas

Department of Physics and Astronomy, Georgia State University, Atlanta, GA 30303, USA; bentz@astro.gsu.edu

Received 2018 April 10; revised 2018 July 17; accepted 2018 August 1; published 2018 September 11

Abstract

We have utilized high-resolution optical *Hubble Space Telescope* images and deep, ground-based near-infrared images to examine the host galaxies of 37 active galactic nuclei (AGNs) with reverberation-based black hole masses. Using two-dimensional image decompositions, we have separated the host galaxy from the bright central AGN, allowing a re-examination of the $M_{\text{BH}}-L_{\text{bulge}}$ and $M_{\text{BH}}-L_{\text{galaxy}}$ relationships and the $M_{\text{BH}}-M_{\text{bulge}}$ and $M_{\text{BH}}-M_{\text{stars}}$ relationships using $V-H$ color to constrain the stellar mass-to-light ratio. We find clear correlations for all of these scaling relationships, and the best-fit correlations are generally in good agreement with the sample of early-type galaxies with M_{BH} from dynamical modeling and the sample of megamasers. We also find good agreement with the expectations from the Illustris simulations, although the agreement with other simulations is less clear because of the different black hole mass ranges that are probed. $M_{\text{BH}}-L_{\text{bulge}}$ is found to have the least scatter, and is therefore the best predictor of M_{BH} among the relationships examined here. Large photometric surveys that rely on automated analysis and forego bulge-to-disk decompositions will achieve more accurate M_{BH} predictions if they rely on $M_{\text{BH}}-M_{\text{stars}}$ rather than $M_{\text{BH}}-L_{\text{galaxy}}$. Finally, we have examined $M_{\text{BH}}/M_{\text{stars}}$ and find a clear trend with black hole mass but not galaxy mass. This trend is also exhibited by galaxies with M_{BH} from dynamical modeling and megamaser galaxies, as well as simulated galaxies from Illustris, rising from $\sim 0.01\%$ at $10^6 M_{\odot}$ to $\sim 1.0\%$ at $10^{10} M_{\odot}$. This scaling should be taken into account when comparing galaxy samples that are not matched in M_{BH} .

Key words: galaxies: active – galaxies: photometry – galaxies: Seyfert – quasars: supermassive black holes

1. Introduction

The discovery that nearly every massive galaxy hosts a supermassive black hole in its nucleus is one of the lasting legacies of the *Hubble Space Telescope* (*HST*). Direct measurements of the masses of these black holes (M_{BH}), using luminous tracers inside the gravitational potential of the invisible central massive object, have led to the discovery of scaling relationships between the black holes and other characteristics of their host galaxies. This is true both for the sample of mostly quiescent galaxies with measurements of M_{BH} from dynamical modeling of stars or gas (e.g., Kormendy & Ho 2013) and for the sample of active galaxies that have measurements of M_{BH} from reverberation mapping (e.g., Bentz & Katz 2015).

Direct black hole mass measurements are time and resource intensive, and they are generally only applicable to galaxies that meet a specific set of criteria. For instance, reverberation mapping is only applicable to broad-lined active galactic nuclei (AGNs), which are rare in the local universe, whereas dynamical modeling is only applicable when the black hole sphere of influence is resolved or nearly so, which is generally only possible out to $\lesssim 100$ Mpc. The resource-intensive nature of these measurements as well as the limitations on the applicability of each technique mean that, in practical terms, the number of direct M_{BH} measurements that may be accumulated over time is necessarily limited. The scaling relationships derived from these direct M_{BH} measurements, however, provide valuable shortcuts for estimating M_{BH} based on less resource-intensive measurements, such as the bulge stellar velocity dispersion (the $M_{\text{BH}}-\sigma_*$ relationship; Ferrarese & Merritt 2000; Gebhardt et al. 2000). As such, direct M_{BH} measurements and the scaling relationships based on them provide the foundation for all other M_{BH} determinations, thereby providing avenues to amass large samples for studying black hole

and galaxy co-evolution across galaxy types and at different look-back times (e.g., Kelly & Merloni 2012; Heckman & Best 2014; Lapi et al. 2014, and references therein).

Scaling relationships between the central black hole and the host galaxy have also become important tools for critical testing of cosmological simulations of dark matter halo mergers (e.g., Hopkins et al. 2010; Degraf et al. 2011; Oogi et al. 2016), numerical investigations of candidate seed black holes (e.g., Lippai et al. 2009; Volonteri & Natarajan 2009; Shirakata et al. 2016), cosmological modeling of galaxy and black hole growth (e.g., Miller et al. 2006; Bonoli et al. 2009; Kim et al. 2011; DeGraf et al. 2015), and investigations into black hole feedback mechanisms (e.g., Ostriker et al. 2010; Kaviraj et al. 2011; Shabala et al. 2011; Steinborn et al. 2015). Accurate measurements of the host-galaxy characteristics of black holes with direct M_{BH} measurements are therefore necessary and valuable. Uncorrected biases or unmitigated scatter in the galaxy measurements can adversely affect the accurate and precise calibration of widely used scaling relationships.

In this work, we focus on characterization of the host galaxies of AGNs with reverberation-based M_{BH} measurements. Using high-resolution *HST* optical images and deep, ground-based near-infrared images, we characterize the photometric properties of the galaxies through two-dimensional image decompositions. We estimate stellar masses based on photometric colors and widely used mass-to-light ratio (M/L) prescriptions. These results then allow us to recalibrate several black hole–galaxy scaling relationships, and to investigate the black hole mass to stellar mass fraction across the sample.

Throughout this work, we adopt a standard Λ CDM cosmology of $H_0 = 72 \text{ km s}^{-1} \text{ Mpc}^{-1}$ with $\Omega_{\Lambda} = 0.7$ and $\Omega_M = 0.3$.

Table 1
Galaxy Sample and Observations

Object	R.A. (hh:mm:ss)	Decl. (°:′:″)	z	Date (yyyy mm dd)	Exp Time (s)	Obs Setup
Mrk 335	00:06:20.2	+20:12:10	0.0258	2011 Sep 20	350.0	WIYN WHIRC H
				2006 Aug 24	2040.0	ACS HRC F550M
Mrk 1501	00:10:31.3	+10:58:30	0.0893	2011 Sep 20	1400.0	WIYN WHIRC H
				2014 Oct 23	2236.0	WFC3 UVIS2 F547M
PG 0026+129	00:29:14.1	+13:16:03	0.1420	2006 Jun 24	2559.8	NICMOS NIC2 F160W
				2007 Jun 06	1445.0	WFPC2 F547M
Mrk 590	02:14:33.3	−00:46:00	0.0264	2012 Jan 13	1500.0	WIYN WHIRC H
				2003 Dec 18	1020.0	ACS HRC F550M
3C 120	04:33:11.1	+05:21:16	0.0330	2011 Sep 20	200.0	WIYN WHIRC H
				2003 Dec 05	1020.0	ACS HRC F550M
Akn 120	05:16:11.1	−00:08:59	0.0327	2012 Jan 13	1000.0	WIYN WHIRC H
				2006 Oct 30	2040.0	ACS HRC F550M
Mrk 6	06:52:12.1	+74:25:37	0.0188	2012 Jan 13	720.0	WIYN WHIRC H
				2014 Nov 06	2620.0	WFC3 UVIS2 F547M
Mrk 79	07:42:33.3	+49:48:35	0.0222	2012 Jan 13	4140.0	WIYN WHIRC H
				2006 Nov 08	2040.0	ACS HRC F550M
PG 0844+349	08:47:42.4	+34:45:04	0.0640	2006 Oct 01	2559.8	NICMOS NIC2 F160W
				2004 May 10	1020.0	ACS HRC F550M
Mrk 110	09:25:13.1	+52:17:11	0.0353	2013 Apr 26	3500.0	WIYN WHIRC H
				2004 May 28	1020.0	ACS HRC F550M
NGC 3227	10:23:31.3	+19:51:54	0.0039	2013 Apr 26	1470.0	WIYN WHIRC H
				2010 Mar 29	2250.0	WFC3 UVIS2 F547M
NGC 3516	11:06:47.5	+72:34:07	0.0088	2012 Jan 13	1625.0	WIYN WHIRC H
				2009 Nov 10	2660.0	WFC3 UVIS2 F547M
SBS 1116+583A	11:18:58.6	+58:03:24	0.0279	2013 Apr 28	6300.0	WIYN WHIRC H
				2010 Jun 06	2510.0	WFC3 UVIS2 F547M
Arp 151	11:25:36.4	+54:22:57	0.0211	2013 Apr 28	3780.0	WIYN WHIRC H
				2010 Apr 09	2450.0	WFC3 UVIS2 F547M
Mrk 1310	12:01:14.1	−03:40:41	0.0196	2013 Apr 27	4500.0	WIYN WHIRC H
				2009 Dec 02	2240.0	WFC3 UVIS2 F547M
NGC 4051	12:03:10.1	+44:31:53	0.0023	2013 Apr 26	3060.0	WIYN WHIRC H
				2010 Jul 17	2340.0	WFC3 UVIS2 F547M
NGC 4151	12:10:33.3	+39:24:21	0.0033	2013 Apr 27	1005.0	WIYN WHIRC H
				2010 Jul 03	2310.0	WFC3 UVIS2 F547M
Mrk 202	12:17:55.6	+58:39:35	0.0210	2013 Apr 28	4800.0	WIYN WHIRC H
				2010 Apr 14	2510.0	WFC3 UVIS2 F547M
NGC 4253	12:18:27.3	+29:48:46	0.0129	2012 Jan 13	1700.0	WIYN WHIRC H
				2010 Jun 21	2270.0	WFC3 UVIS2 F547M
PG 1226+023	12:29:07.7	+02:03:09	0.1583	2013 Apr 28	2250.0	WIYN WHIRC H
				2007 Jan 17	2040.0	ACS HRC F550M
PG 1229+204	12:32:04.4	+20:09:29	0.0630	2003 Nov 30	2559.8	NICMOS NIC2 F160W
				2006 Nov 20	2040.0	ACS HRC F550M
NGC 4593	12:39:39.4	−05:20:39	0.0090	2013 Apr 27	960.0	WIYN WHIRC H
				2010 Jul 10	2240.0	WFC3 UVIS2 F547M
NGC 4748	12:52:12.1	−13:24:53	0.0146	2013 Apr 27	3600.0	WIYN WHIRC H
				2010 Jun 28	2250.0	WFC3 UVIS2 F547M
PG 1307+085	13:09:47.5	+08:19:48	0.1550	2007 Jan 23	2559.8	NICMOS NIC2 F160W
				2007 Mar 21	1445.0	WFPC2 F547M
Mrk 279	13:53:03.3	+69:18:30	0.0305	2013 Apr 27	2300.0	WIYN WHIRC H
				2003 Dec 07	1020.0	ACS HRC F550M
PG 1411+442	14:13:48.5	+44:00:14	0.0896	2006 Nov 27	2559.8	NICMOS NIC2 F160W
				2006 Nov 11	2040.0	ACS HRC F550M
PG 1426+015	14:29:07.7	+01:17:06	0.0866	2007 Mar 03	2559.8	NICMOS NIC2 F160W
				2007 Mar 20	1445.0	WFPC2 F547M
Mrk 817	14:36:22.2	+58:47:39	0.0315	2013 Apr 26	3520.0	WIYN WHIRC H
				2003 Dec 08	1020.0	ACS HRC F550M
PG 1613+658	16:13:57.6	+65:43:10	0.1290	2011 Sep 19	1260.0	WIYN WHIRC H
				2006 Nov 12	2040.0	ACS HRC F550M
PG 1617+175	16:20:11.1	+17:24:28	0.1124	2006 Jul 09	2559.8	NICMOS NIC2 F160W
				2007 Mar 19	1445.0	WFPC2 F547M
PG 1700+518	17:01:25.3	+51:49:20	0.2920	2006 Oct 05	2559.8	NICMOS NIC2 F160W
				2006 Nov 16	2040.0	ACS HRC F550M
3C 390.3	18:42:09.9	+79:46:17	0.0561	2013 Apr 26	3060.0	WIYN WHIRC H

Table 1
(Continued)

Object	R.A. (hh:mm:ss)	Decl. (°:′:″)	z	Date (yyyy mm dd)	Exp Time (s)	Obs Setup
Zw 229-015	19:05:26.3	+42:27:40	0.0279	2004 Mar 31	1020.0	ACS HRC F550M
				2011 Sep 20	2000.0	WIYN WHIRC H
				2014 Nov 13	2320.0	WFC3 UVIS2 F547M
NGC 6814	19:42:41.4	−10:19:25	0.0052	2011 Sep 20	1200.0	WIYN WHIRC H
				2010 May 06	2240.0	WFC3 UVIS2 F547M
Mrk 509	20:44:10.1	−10:43:25	0.0344	2011 Sep 19	385.0	WIYN WHIRC H
				2007 Apr 01	1445.0	WFPC2 F547M
PG 2130+099	21:32:28.3	+10:08:19	0.0630	2011 Sep 19	1800.0	WIYN WHIRC H
				2003 Oct 21	1020.0	ACS HRC F550M
NGC 7469	23:03:16.2	+08:52:26	0.0163	2011 Sep 19	300.0	WIYN WHIRC H
				2009 Nov 11	2240.0	WFC3 UVIS2 F547M

2. Observations

As part of our ongoing work with the reverberation sample of AGNs, high-resolution medium-band V observations were obtained with the *HST*. We have also recently collected deep, ground-based near-infrared imaging for a number of these galaxies at the WIYN observatory. We restrict our analysis here to the sample of 37 galaxies for which we have imaging in both the optical and near-infrared. Table 1 lists the sample and details of the observations, which we describe below.

2.1. Optical Imaging

HST imaging of the galaxies in our sample was acquired with the following instrument configurations: the Advanced Camera for Surveys (ACS) High Resolution Channel (HRC) through the F550M filter, the Wide Field Planetary Camera 2 (WFPC2) with the F547M filter, and the Wide Field Camera 3 (WFC3) through the F547M filter. The medium-band V filters were specifically chosen to avoid strong emission lines from the AGN and to sample a flat portion of the underlying host-galaxy spectrum. The details of these observations and the post-processing are described by Bentz et al. (2009a, 2013).

We also present here new WFC3 F547M images of eight galaxies in the sample (*HST* GO-11661 and GO-13816, PI Bentz). Three had not been previously observed, while prior imaging of five galaxies with the ACS HRC provided a field of view ($29''.0 \times 25''.0$) that was too narrow to capture their extended morphologies. WFC3 provides a $2''.7 \times 2''.7$ field of view that is well matched to the galaxies in our sample, and a high spatial resolution with a pixel scale of $0''.04$. Each galaxy was observed for a single orbit, with a two-point dither pattern to fill in the gap between the detectors. At each point in the dither, a short and long exposure were obtained. The short exposures ensure an unsaturated measurement of the bright central AGN at each position, while the long exposures provide more depth for resolving the fainter, extended host galaxy.

The pipeline-reduced images were corrected for cosmic rays with LACosmic (van Dokkum 2001). Taking advantage of the linear nature of CCDs, we corrected for saturation of the AGN in the long exposures by clipping out the saturated pixels in the long exposures and replacing them with the same pixels from the short exposures taken at the same dither position, scaled up by the exposure time ratio. The individual exposures were then drizzled to a common reference and combined with AstroDrizzle.

2.2. Near-infrared Imaging

Near-infrared imaging of 29 reverberation-mapped AGN host galaxies was obtained between fall 2011 and spring 2013 with the WIYN High-Resolution Infrared Camera (WHIRC) at the WIYN 3.5 m telescope.¹ The camera is a Raytheon Virgo HgCdTe with a pixel scale of $0''.0986$ and a field of view of $202'' \times 202''$. While broadband J , H , and K_s images were obtained for a subset of the sample, the majority of the observations were devoted to H -band images and we report those here.

The typical observing sequence involved many short observations of each target with a generous dither pattern between observations. This allowed for the removal of strong fringing in the H band, as well as bad pixels and cosmic rays.

Images were reduced in IRAF² following standard procedures. Strong fringing is a known problem for H -band images taken with WHIRC. We were able to correct for this effect by first median-combining a large number of dithered observations of a target, with each image scaled by the median sky level. Then we created a fringe mask from this combined image with the IRAF task `objmasks`. Finally, we used the mask with the `rmfringe` task to correct each image. After correcting for fringing, we computed the pixel offsets between dithered images, subtracted the mean sky background, and shifted and combined all of the images. For the final image of each object, we added back the average sky background that had been subtracted in the previous step, to ensure that the image statistics would be properly handled in the fitting process. In Figure 1 we show the final H -band images for three of our targets in comparison to the Two Micron All Sky Survey (2MASS; Skrutskie et al. 2006) H -band images for the same galaxies. The improvement in depth and spatial resolution provided by the WHIRC images is immediately apparent, allowing for detection and characterization of faint surface brightness features, as well as better separation of distinct photometric components.

We supplemented this sample with *HST* Near-Infrared Camera and Multi-Object Spectrometer (NICMOS) observations of eight additional PG quasars with the NIC2 camera

¹ The WIYN Observatory is a joint facility of the University of Wisconsin-Madison, Indiana University, the National Optical Astronomy Observatory and the University of Missouri.

² IRAF is distributed by the National Optical Astronomy Observatory, which is operated by the Association of Universities for Research in Astronomy (AURA) under a cooperative agreement with the National Science Foundation.

Table 2
Galaxy Decompositions

Object	m_V (mag)	m_H (mag)	r (arcsec)	n	q	PA (°E of N)	Note
Mrk 335	16.59	13.26	1.59	2.9	0.85	−72.8	Bulge
	15.93	13.88	2.89	1.0	0.98	66.0	Disk
Mrk 1501	17.78	16.08	0.25	1.0	0.58	1.9	Inner disk
	17.49	14.22	1.64	1.1	0.81	−73.3	Bulge
	16.10	14.72	14.44	1.0	0.56	1.6	Disk
PG 0026+129	17.22	15.46	1.89	4.0	0.78	−83.6	Bulge
Mrk 590	16.07	12.78	0.90	1.4	0.66	−35.5	Bulge
	16.07	12.79	1.32	0.4	0.95	−88.2	Barlens
	14.28	11.03	5.43	1.0	0.89	35.1	Disk
3C 120	17.10	12.76	1.19	1.4	0.92	−76.6	Bulge
	15.92	12.74	6.54	1.0	0.62	−59.1	Disk
Akn 120	15.15	11.93	0.83	3.9	0.88	−14.5	Bulge
	14.87	12.06	5.10	1.0	0.81	20.8	Disk
Mrk 6	15.32	11.30	2.89	1.3	0.82	−51.0	Bulge
	14.24	12.26	15.72	1.0	0.61	−49.9	Disk
	5.95, 4.13	...	0.13	−57.2	Dust lane-inner
Mrk 79	15.72	12.30	2.44	3.3	0.88	59.1	Bulge
	15.79	13.58	14.92	0.3	0.11	58.8	Bar
	14.43	11.84	12.36	1.0	0.79	29.1	Disk
PG 0844+349	17.50	14.34	0.86	4.0	0.86	−1.9	Bulge
	16.95	14.45	2.91	1.0	0.78	47.0	Disk
Mrk 110	17.95	13.74	0.43	1.6	0.93	−50.4	Bulge
	16.44	13.47	2.83	1.0	0.91	89.5	Disk
NGC 3227	13.95	9.77	2.69	2.5	0.61	−17.1	Bulge
	16.72	11.84	0.44	0.3	0.52	43.6	Bar
	11.04	8.03	58.39	1.0	0.42	−26.2	Disk
NGC 3516	13.38	10.10	2.15	1.3	0.79	53.2	Bulge
	15.00	12.12	8.13	0.3	0.41	−17.5	Bar
	13.59	10.94	9.11	0.8	0.71	−12.3	Barlens
	12.55	11.19	32.75	1.0	0.79	39.2	Disk
SBS 1116+583A	20.37	15.43	0.33	1.1	0.80	61.5	Bulge
	20.22	14.95	0.96	0.3	0.93	77.1	Barlens
	19.88	14.07	3.42	0.5	0.25	69.2	Bar
	17.62	13.26	5.00	1.0	0.87	67.6	Disk
Arp 151	15.73	12.39	2.37	4.1	0.78	−25.3	Bulge
	16.86	14.13	4.44	1.0	0.28	−22.6	Disk
Mrk 1310	16.43	13.20	1.88	3.0	0.77	−42.4	Bulge
	17.62	14.76	8.00	1.0	1.00	0.0	Ring
	4.76, 4.90	...	0.65	−42.4	Ring-inner
	0.87, 4.11	...	0.75	−52.2	Ring-outer
	15.28	13.15	5.72	1.0	0.73	−37.6	Disk
NGC 4051	14.70	12.00	0.94	0.7	0.75	−40.2	Bulge
	14.00	10.14	6.00	1.6	0.46	−50.8	Bar
	10.11	8.43	89.67	1.0	0.70	−58.5	Disk
NGC 4151	14.91	13.35	0.88	2.2	0.41	55.9	Bar
	13.82	10.42	2.05	0.9	0.91	−70.5	Bulge
	12.60	9.40	8.50	0.6	0.87	39.5	Barlens
	11.09	8.77	58.39	1.0	0.61	−47.2	Disk
Mrk 202	17.18	13.56	0.54	2.7	0.80	−54.7	Bulge
	18.21	14.90	4.00	1.0	1.00	0.0	Ring
	2.15, 1.72	...	0.89	17.7	Ring-inner
	0.70, 1.86	...	0.76	−67.4	Ring-outer
	15.64	13.47	6.99	1.0	0.79	−52.9	Disk
NGC 4253	17.62	14.75	0.19	0.1	0.62	−85.3	Nucleus
	16.46	12.97	1.42	1.1	0.56	−56.8	Bulge
	14.68	11.77	7.82	0.5	0.30	−71.2	Bar
	13.51	11.88	16.17	1.0	0.84	83.0	Disk
PG 1226+023	14.75	13.20	0.94	3.8	0.85	64.8	Bulge
PG 1229+204	16.13	13.05	2.69	4.0	0.87	−18.6	Bulge
	16.79	14.56	7.48	1.0	0.32	34.8	Disk
NGC 4593	15.17	12.47	2.56	0.1	0.73	−65.8	Barlens
	13.20	9.85	7.65	1.4	0.73	−84.6	Bulge
	13.66	10.61	35.13	0.3	0.24	55.8	Bar

Table 2
(Continued)

Object	m_V (mag)	m_H (mag)	r (arcsec)	n	q	PA (°E of N)	Note
NGC 4748	11.51	9.50	74.33	1.0	0.51	65.9	Disk
	17.36	13.63	0.70	0.1	0.78	50.4	Nucleus
	14.70	10.96	5.82	2.3	0.76	49.2	Bulge
PG 1307+085	13.99	13.77	16.80	1.0	0.69	77.4	Disk
	16.17	13.96	18.13	4.0	0.78	−67.0	Bulge
	Mrk 279	16.25	12.32	1.7	0.56	32.7	Bulge
PG 1411+442	15.16	12.20	5.34	1.0	0.56	32.9	Disk
	16.74	13.80	2.01	4.0	0.68	−10.8	Bulge
	PG 1426+015	16.68	13.88	4.0	0.53	−53.5	Bulge
Mrk 817	16.38	13.90	6.41	1.0	0.39	52.1	Disk
	17.68	13.24	0.90	1.0	0.82	−40.6	Bulge
	17.45	14.04	5.57	0.1	0.24	−72.2	Bar
PG 1613+658	14.29	11.70	7.93	1.0	0.81	−66.8	Disk
	15.92	12.81	4.24	2.4	0.79	−21.7	Bulge
	PG 1617+175	17.33	15.19	4.0	0.89	−67.7	Bulge
PG 1700+518	17.92	15.24	1.98	4.0	0.66	37.5	Bulge
	3C 390.3	17.18	13.86	1.7	0.74	72.0	Bulge
	16.86	13.61	2.80	1.0	0.96	−24.8	Disk
Zw 229-015	17.10	13.92	0.75	1.1	0.72	48.1	Bulge
	16.80	13.49	4.34	0.3	0.54	38.1	Bar
	15.65	14.74	13.25	1.0	0.60	44.8	Disk
NGC 6814	17.28	13.85	13.42	1.0	0.56	42.5	Ring
	19.03, 14.97	...	0.70	43.7	Ring-inner
	8.26, 10.66	...	0.54	44.0	Ring-outer
Mrk 509	17.09	12.79	1.91	1.8	0.47	21.1	Inner bar
	14.95	11.27	1.84	1.7	0.94	10.1	Bulge
	14.94	10.76	6.17	0.4	0.64	25.7	Bar
PG 2130+099	11.22	8.84	44.09	1.0	0.98	25.0	Disk
	15.25	12.41	2.19	1.0	0.67	82.5	Disk
	16.98	13.52	4.50	1.0	0.44	−70.3	Ring
NGC 7469	3.45, 1.05	...	0.60	76.2	Ring-inner
	2.21, 9.57	...	0.36	21.0	Ring-outer
	17.90	13.67	0.54	5.1	0.51	64.2	Bulge
NGC 7469	16.53	13.52	4.34	1.0	0.55	47.1	Disk
	15.15	11.16	2.94	0.3	0.70	−61.3	Bulge
	14.92	11.19	4.00	1.0	0.90	13.0	Ring
NGC 7469	3.09, 3.46	...	0.36	45.8	Ring-inner
	1.18, 1.18	...	0.76	58.2	Ring-outer
	16.82	13.32	0.51	0.2	0.67	68.4	Inner disk
NGC 7469	14.12	11.17	10.42	0.2	0.56	−58.0	Inner disk
	15.65	12.73	33.84	1.0	0.81	−56.9	Disk

through the F160W filter. Details of these observations are described by Veilleux et al. (2009). Drizzled and combined images were downloaded from MAST. For each image, we added back the subtracted sky background as recorded in the header, and then multiplied each image by the exposure time to return the image units to counts.

3. Surface Brightness Fits

Two-dimensional surface brightness fits to the AGN host galaxy images were carried out using the software GALFIT (Peng et al. 2002, 2010). GALFIT allows the user to model surface brightness features with a variety of analytical models. We utilized the general Sérsic (1968) profile to fit the various photometric components of each galaxy. This particular

function has the form

$$\Sigma(r) = \Sigma_e \exp \left[-\kappa \left(\left(\frac{r}{r_e} \right)^{1/n} - 1 \right) \right], \quad (1)$$

where Σ_e is the pixel surface brightness at the effective radius r_e . An exponential disk profile is simply a Sérsic profile with an index of $n = 1$. Bulges typically have $n > 1$, with the de Vaucouleurs (1948) profile being a special case with $n = 4$. Bars, on the other hand, typically have $n < 1$. In the few cases where a galaxy displayed a ring or a strong dust lane, we utilized the truncation function to truncate the inner and/or outer regions of a Sérsic profile with $n = 1$ to represent the ring. For these profiles, there are two quoted radii for each truncation function, which are the break radius and the softening length.

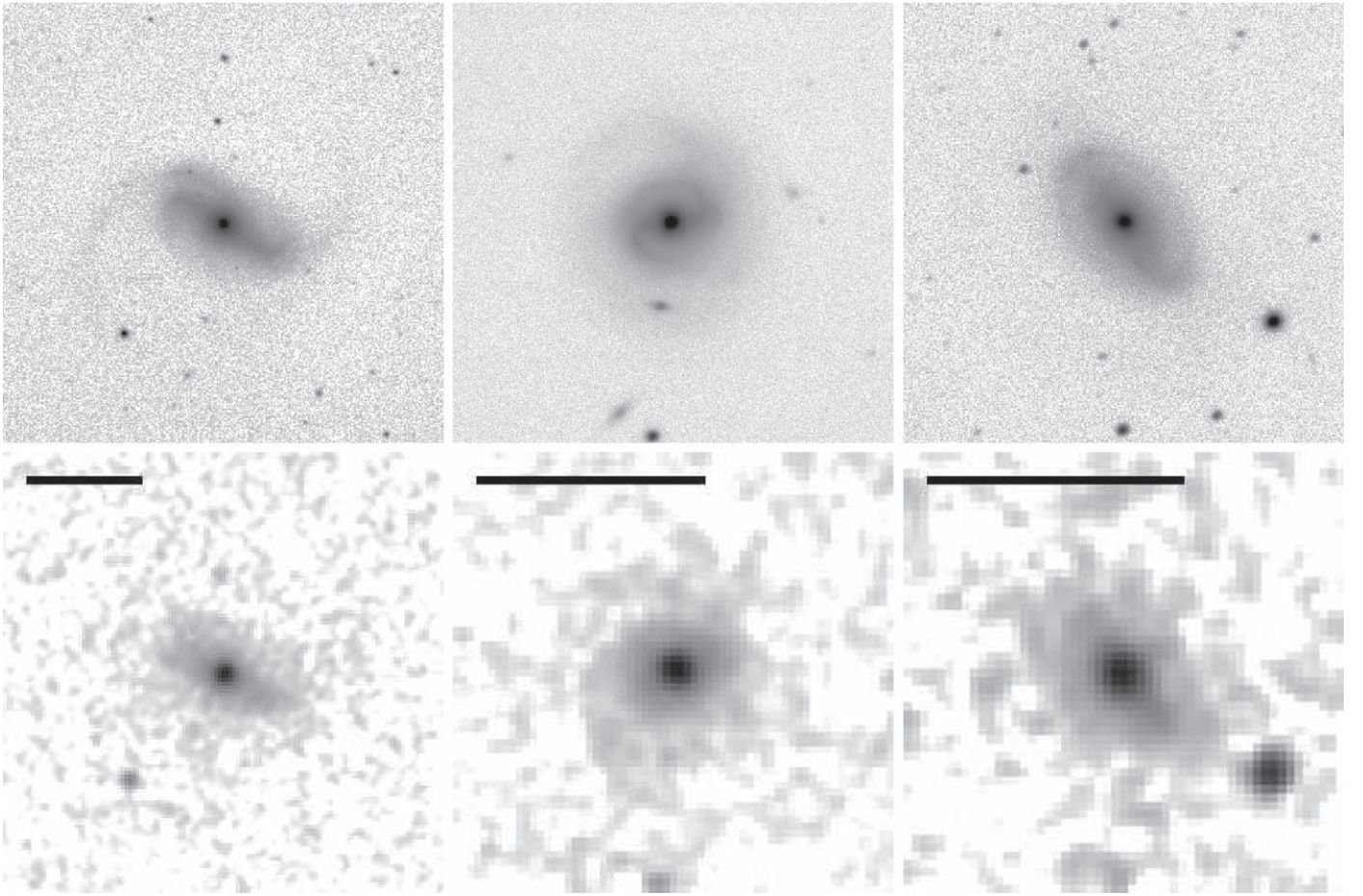


Figure 1. Top row: WIYN WHIRC H -band image negatives of the Seyfert galaxies Mrk 79 (left), Mrk 817 (center), and Zw 229–015 (right). All images are oriented with north up and east to the left. Note that we have successfully removed the fringing that is typical of this instrument in the H band, and that there is a high level of morphological detail captured in each galaxy. Bottom row: 2MASS H -band image negatives of the same galaxies from the 2MASS Extended Source Catalog (Jarrett et al. 2000). For each object, the displayed field of view for the 2MASS image matches the WIYN image, and the scale bars are $30''$ in length. The shallow depth and poorer spatial resolution of the 2MASS imaging loses many of the morphological details of the host galaxies, but these details are clearly captured in the WIYN images.

Fits to many of the optical *HST* images have already been published by Bentz et al. (2009a, 2013). Fits to the new WFC3 images were carried out following similar procedures. The point-spread function (PSF) was modeled by StarFit (Hamilton 2014) in an attempt to better account for slight changes in the PSF width due to telescope breathing. StarFit begins with a TinyTim PSF model (Krist 1993) and attempts to match the telescope focus by fitting the PSF to a source in the field. Most of the galaxies did not have a suitable field star in the frame to be used as a PSF model, so we used the StarFit model derived from a star in the field of NGC 3516 as the PSF model for all eight galaxies. While this provided a slight improvement over using basic TinyTim PSF models, we still found that in several cases we needed to supplement the PSF model with a narrow Sérsic profile to properly model the AGN in each galaxy nucleus. Without the addition of this component, the Sérsic profiles for the bulge would run up to an unrealistic index of $n > 10$, and would often reach the default maximum value of $n = 20$. Such profiles are extremely peaky with very broad wings, effectively mimicking an unresolved point source and the background sky. Whenever this occurred, we added a narrow (FWHM $\lesssim 1$ pixel) Sérsic on top of the PSF model at the location of the AGN. The addition of this profile always

resulted in realistic values for all other model components in the image, allowing all the model components to remain unfixed during the fitting. The surface brightness profile of each galaxy was then fit with a bulge and a disk model, with additional model parameters (such as a bar, barlens, or ring) being added when necessary based on inspection of the image and the residuals of the model.

For the near-infrared WHIRC images, our fitting process began by constructing a PSF image from an isolated field star. This first step involved analyzing a small portion of each image centered on the star. The background sky was modeled as a tilted plane, and we fit multiple Gaussians to the star (typically four or five) with unrestricted shape parameters and initial conditions of widths graduated in size. We also allowed for a single Fourier term to provide an asymmetry in the light distribution of each Gaussian, although we first arrived at a good set of model parameters before turning this option on in the final fitting step. The end result of each PSF model image is a residual pattern (image minus model) that does not retain any “bulls-eye” or other regular pattern, and is simply consistent with noise. These models, excluding the sky component, were then used as the PSF images for fitting the galaxy.

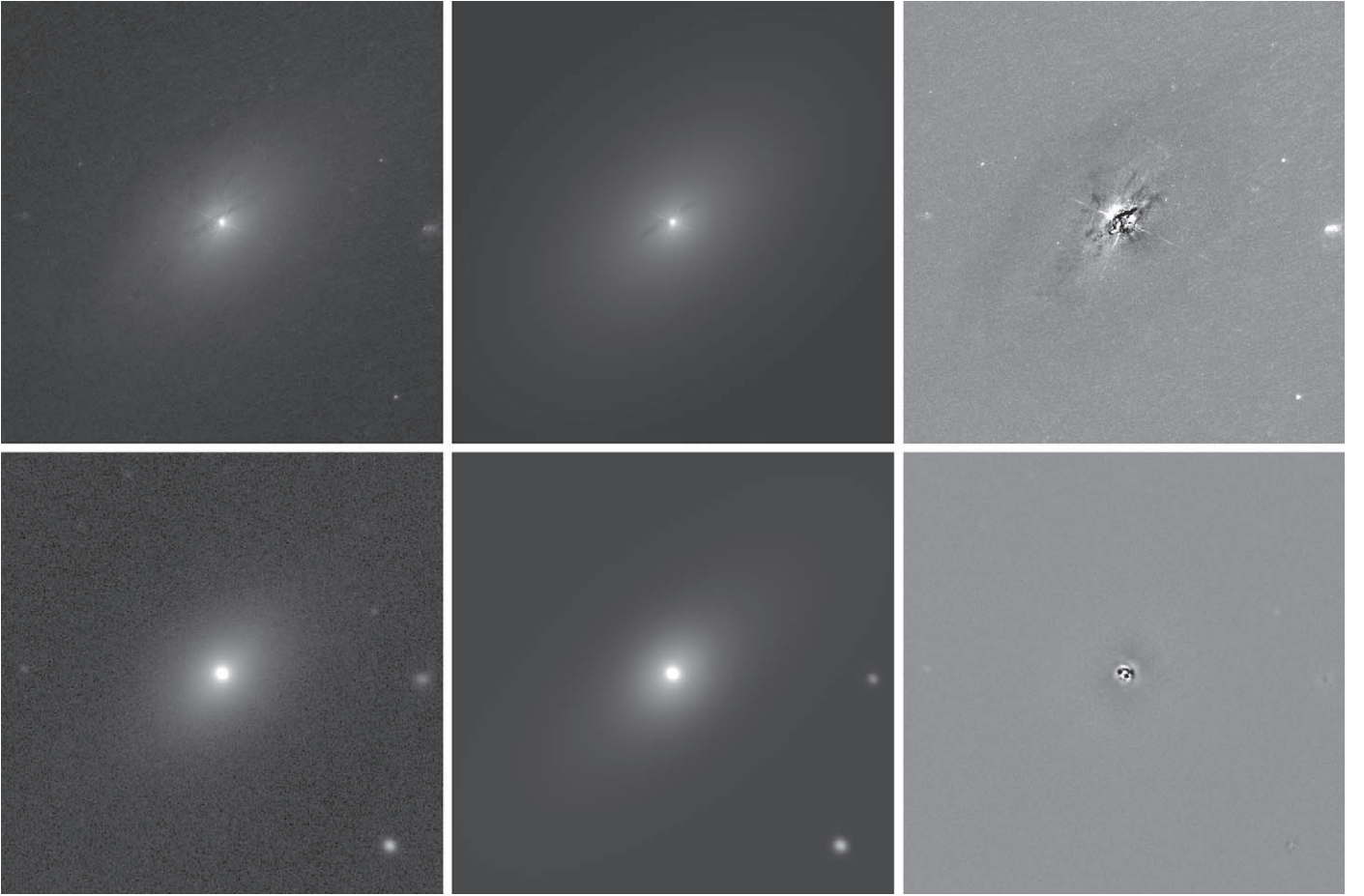


Figure 2. Two-dimensional surface brightness decompositions of Mrk 6, with the top row showing the medium-*V* *HST* image and the lower row showing the *H*-band WHIRC image. In the three panels of each row, we show the image (left), the model that was fit to the image (center), and the residuals after subtracting the model from the image (right). The images and models are displayed with a logarithmic stretch, and the residuals are displayed with a linear stretch centered around zero counts. The fields displayed are $1' \times 1'$ and are oriented with north up and east to the left.

The fits of the WHIRC *H*-band images were guided by the solutions determined from the optical *HST* images because of their superior sensitivity and spatial resolution and lower sky background. The host-galaxy components in the WHIRC images were constrained to have the same characteristic radii as had been found in the optical images, scaled by the difference in the pixel scales. Furthermore, the indices of the Sérsic profiles were constrained to the values determined from the optical images. In a few cases, unsatisfactory fits of the WHIRC images led us to revisit and refine our previously published fits to an *HST* image, and these new fits to the optical images were then used to guide the fits to the WHIRC images. In all cases, the final adopted fits in both the optical and near-infrared bands agreed, both in the number of photometric models and their shape parameters. The sky background was again fit as a tilted plane, and the AGN and multiple field stars were fit with the PSF image. Field stars that were not fit were masked out. Because of the non-photometric conditions throughout most of our WHIRC observations, we adopted *H*-band magnitudes for as many field stars as possible in each image from 2MASS. The final zero-point of each WHIRC image was set by minimizing the differences between the reported 2MASS magnitudes and the GALFIT magnitudes of the field stars. Figure 2 shows the *HST* and WHIRC images for a typical galaxy in our sample, Mrk 6, as well as the surface brightness models fit to each image and the residuals of the fits.

While the Sérsic indices for the surface brightness components fit to the optical *HST* images were generally allowed to remain free parameters, we followed a slightly different procedure for the analysis of the eight PG quasars included in the sample of Veilleux et al. (2009). At first, we intended to match the procedure described by Veilleux et al. so that we could adopt the galaxy magnitudes they report, but in the end we found that we preferred a modified version of the procedure, and we thus re-fit all the NICMOS images ourselves.

As with the other galaxies, we began with the optical images. These were all WFPC2 or ACS HRC images, and the small field of view did not allow for a StarFit PSF model to be built from a suitably bright field star. The PSF was instead modeled with TinyTim (Krist 1993) and we again found that we needed to add an additional narrow Sérsic component on top of the PSF to help avoid mismatch from spacecraft breathing. Each galaxy was fit with either a single Sérsic component with $n = 4$, or with an exponential disk and a Sérsic component with $n = 4$, depending on whether our previous fits and those reported by Veilleux et al. (2009) found evidence for a disk or not. Faint field stars and galaxies in the images were fit simultaneously with the AGN and its host galaxy, rather than masked out. Once a good fit was obtained in the optical image (all of which have finer pixel scales and marginally larger fields of view than the NIC2 camera), we turned to the fitting of the

Table 3
Bulge and Galaxy Magnitudes and Luminosities

Object	D (Mpc)	V_{bulge} (mag)	V_{galaxy} (mag)	$\log L_{\text{bulge}} (V)$ (L_{\odot})	$\log L_{\text{galaxy}} (V)$ (L_{\odot})	H_{bulge} (mag)	H_{galaxy} (mag)	$\log L_{\text{bulge}} (H)$ (L_{\odot})	$\log L_{\text{galaxy}} (H)$ (L_{\odot})
Mrk 335	109.5 \pm 7.1	16.59	15.42	9.409 \pm 0.098	9.861 \pm 0.098	13.25	12.76	10.117 \pm 0.098	10.312 \pm 0.098
Mrk 1501	402.5 \pm 7.5	17.22	15.40	10.325 \pm 0.082	11.055 \pm 0.082	14.17	13.53	10.872 \pm 0.082	11.129 \pm 0.082
PG 0026+129	653.1 \pm 7.7	17.03	17.03	10.868 \pm 0.081	10.868 \pm 0.081	15.30	15.30	10.840 \pm 0.081	10.840 \pm 0.081
Mrk 590	112.1 \pm 7.1	16.07	13.89	9.633 \pm 0.097	10.494 \pm 0.097	12.76	10.65	10.333 \pm 0.097	11.177 \pm 0.097
3C 120	140.9 \pm 7.1	16.38	14.85	9.730 \pm 0.091	10.327 \pm 0.091	12.62	11.86	10.587 \pm 0.091	10.891 \pm 0.091
Akn 120	139.6 \pm 7.1	14.89	13.95	10.311 \pm 0.091	10.670 \pm 0.091	11.87	11.18	10.879 \pm 0.091	11.154 \pm 0.091
Mrk 6	80.6 \pm 7.1	14.97	13.55	9.770 \pm 0.111	10.339 \pm 0.111	11.24	10.86	10.658 \pm 0.111	10.808 \pm 0.111
Mrk 79	94.0 \pm 7.1	15.64	13.80	9.657 \pm 0.103	10.375 \pm 0.103	12.27	11.14	10.376 \pm 0.103	10.830 \pm 0.103
PG 0844+349	279.4 \pm 7.3	17.40	16.35	9.903 \pm 0.083	10.330 \pm 0.083	14.20	13.50	10.543 \pm 0.083	10.823 \pm 0.083
Mrk 110	150.9 \pm 7.1	18.00	16.21	9.130 \pm 0.090	9.823 \pm 0.090	13.74	12.84	10.198 \pm 0.090	10.557 \pm 0.090
NGC 3227	23.5 \pm 2.4	13.92	10.93	9.105 \pm 0.119	10.301 \pm 0.119	9.76	7.80	10.184 \pm 0.119	10.970 \pm 0.119
NGC 3516	37.1 \pm 7.0	13.30	11.74	9.755 \pm 0.182	10.379 \pm 0.182	10.09	9.34	10.448 \pm 0.182	10.747 \pm 0.182
SBS 1116+583A	118.5 \pm 7.1	18.50	15.48	8.696 \pm 0.095	9.907 \pm 0.095	15.42	12.60	9.315 \pm 0.095	10.443 \pm 0.095
Arp 151	89.2 \pm 7.0	15.71	15.39	9.561 \pm 0.105	9.691 \pm 0.105	12.38	12.18	10.287 \pm 0.105	10.367 \pm 0.105
Mrk 1310	82.7 \pm 7.0	16.37	14.81	9.230 \pm 0.109	9.856 \pm 0.109	13.19	12.41	9.899 \pm 0.109	10.211 \pm 0.109
NGC 4051	17.1 \pm 3.4	14.70	10.07	8.515 \pm 0.190	10.368 \pm 0.190	11.99	8.18	9.016 \pm 0.190	10.539 \pm 0.190
NGC 4151	16.6 \pm 3.3	13.78	10.72	8.858 \pm 0.190	10.083 \pm 0.190	10.41	8.12	9.622 \pm 0.190	10.538 \pm 0.190
Mrk 202	88.9 \pm 7.1	17.15	15.30	8.982 \pm 0.106	9.725 \pm 0.106	13.55	12.61	9.818 \pm 0.106	10.193 \pm 0.106
NGC 4253	54.4 \pm 7.0	16.44	13.10	8.835 \pm 0.138	10.171 \pm 0.138	12.96	10.86	9.628 \pm 0.138	10.470 \pm 0.138
PG 1226+023	735.7 \pm 7.7	14.81	14.77	11.882 \pm 0.081	11.882 \pm 0.081	13.20	13.20	11.781 \pm 0.081	11.781 \pm 0.081
PG 1229+204	274.9 \pm 7.3	16.04	15.59	10.430 \pm 0.083	10.619 \pm 0.083	12.91	12.67	11.045 \pm 0.083	11.142 \pm 0.083
NGC 4593	37.3 \pm 7.5	13.17	11.12	9.812 \pm 0.192	10.631 \pm 0.192	9.84	8.66	10.553 \pm 0.192	11.024 \pm 0.192
NGC 4748	61.6 \pm 7.0	14.58	13.39	9.688 \pm 0.127	10.165 \pm 0.127	10.94	10.77	10.546 \pm 0.127	10.611 \pm 0.127
PG 1307+085	718.7 \pm 7.7	16.07	16.07	11.339 \pm 0.081	11.339 \pm 0.081	13.81	13.81	11.514 \pm 0.081	11.514 \pm 0.081
Mrk 279	129.7 \pm 7.1	16.30	14.83	9.673 \pm 0.093	10.246 \pm 0.093	12.31	11.49	10.638 \pm 0.093	10.964 \pm 0.093
PG 1411+442	398.2 \pm 7.4	16.69	16.71	10.511 \pm 0.082	10.511 \pm 0.082	13.67	13.67	11.062 \pm 0.082	11.062 \pm 0.082
PG 1426+015	383.9 \pm 7.4	16.55	15.63	10.543 \pm 0.082	10.909 \pm 0.082	13.74	13.00	11.002 \pm 0.082	11.299 \pm 0.082
Mrk 817	134.2 \pm 7.1	17.69	14.22	9.123 \pm 0.092	10.519 \pm 0.092	13.24	11.37	10.297 \pm 0.092	11.044 \pm 0.092
PG 1613+658	588.4 \pm 7.6	15.91	15.87	11.220 \pm 0.081	11.220 \pm 0.081	12.79	12.79	11.750 \pm 0.081	11.750 \pm 0.081
PG 1617+175	507.4 \pm 7.5	17.18	17.18	10.556 \pm 0.081	10.556 \pm 0.081	15.05	15.05	10.722 \pm 0.081	10.722 \pm 0.081
PG 1700+518	1463.3 \pm 8.4	17.90	17.92	11.417 \pm 0.080	11.417 \pm 0.080	15.08	15.08	11.616 \pm 0.080	11.616 \pm 0.080
3C 390.3	243.5 \pm 7.2	17.05	16.09	9.944 \pm 0.084	10.313 \pm 0.084	13.82	12.94	10.576 \pm 0.084	10.929 \pm 0.084
Zw 229-015	120.2 \pm 7.2	16.93	14.82	9.342 \pm 0.095	10.186 \pm 0.095	13.89	12.38	9.940 \pm 0.095	10.547 \pm 0.095
NGC 6814	21.8 \pm 7.0	14.47	10.66	8.823 \pm 0.289	10.346 \pm 0.289	11.18	8.47	9.549 \pm 0.289	10.635 \pm 0.289
Mrk 509	147.0 \pm 7.1	...	14.87	...	10.344 \pm 0.090	...	12.05	...	10.849 \pm 0.090
PG 2130+099	274.7 \pm 7.3	17.77	16.15	9.739 \pm 0.083	10.395 \pm 0.083	13.65	12.82	10.750 \pm 0.083	11.082 \pm 0.083
NGC 7469	68.8 \pm 7.0	16.66	12.29	8.954 \pm 0.119	10.701 \pm 0.119	13.29	9.82	9.702 \pm 0.119	11.088 \pm 0.119

NICMOS images. The NICMOS PSF was modeled by TinyTim and was subsampled by a factor of 5, and the galaxy model components were adopted from the optical images, scaled to the proper size and held fixed during the fitting of the NICMOS images, as we did with the WHIRC images. The final parameters for the adopted fits are listed in Table 2.

4. Galaxy Characteristics

The GALFIT models described in the previous section constrain the observed magnitudes of the individual photometric components of the host galaxies, which are generally, but not always, related to kinematic components of the galaxy. The fitting process that we adopted allows for a direct comparison of the colors of individual components (e.g., disks, bulges, bars), or the components can be combined to investigate the total magnitude of a galaxy in each passband as well as the overall galaxy color.

4.1. Final Photometry

The optical *HST* magnitudes represent a few different medium-band *V* filters rather than a true broadband Johnson filter. For each object, we used SYNPHOT and a reddened,

redshifted galaxy spectrum to determine the color difference between the filter used for the optical *HST* observations and a broadband *V* filter. We adopted the elliptical galaxy template spectrum of Kinney et al. (1996) for these calculations, but the use of an Sa or Sc galaxy spectrum does not significantly change our results. The color differences are small, $-0.05 < m_V - m_{HST} < 0.13$ mag. Similarly, we determined the difference between the *F160W* magnitudes from the NICMOS images and a “true” *H*-band magnitude using SYNPHOT and the tabulated passband for the *H* filter provided on the WHIRC filters webpage.³ These corrections were slightly larger in magnitude and were always in the same direction, showing a slight bias between the two filters, $-0.15 < m_H - m_{F160W} < -0.12$ mag.

The *V* and *H* magnitudes were then corrected for Galactic extinction along the line of sight based on the values determined from the Schlafly & Finkbeiner (2011) recalibration of the Schlegel et al. (1998) dust map of the Milky Way. Table 3 gives the extinction-corrected *V*- and *H*-equivalent apparent magnitudes for the integrated galaxies and for their bulges.

³ <https://www.noao.edu/kpno/manuals/whirc/filters.html>

Based on our previous experience with GALFIT as well as comparison of our fitting results with those of Veilleux et al. (2009) for several of the PG objects, we assume a typical uncertainty of 0.20 mag for the integrated magnitudes of the galaxies. We also assume a typical uncertainty of 0.20 mag for the integrated magnitudes of the bulge components on their own. This is not to say that all the uncertainty is in the bulges, but rather that GALFIT does a good job of recovering the total galaxy flux, even if there is some ambiguity in how the light is divided between the various photometric components.

4.2. $V - H$ Colors

The galaxies in our sample span a range of distances covering $0.0 < z < 0.3$. We used SYNPHOT to determine k -corrections for each galaxy in V and H so that we could compare $z = 0$ -equivalent photometry and galaxy colors. In H , the relatively flat spectral energy distribution (SED) of a galaxy gives rise to small corrections ranging from $-0.075 < k_H < -0.003$ mag with a median of $k_H = -0.028$ mag. In V , however, there is significantly more structure to a galaxy SED, so the galaxies with the largest redshifts in our sample ($z = 0.1$ – 0.3) have $k_V > 0.2$ mag. The median is significantly smaller, however, at $k_V = 0.061$ mag.

After applying the k -corrections, we derive the $V - H$ colors, both for the integrated light of the galaxy, which we report in Table 4, as well as for each individual component (e.g., bulge, bar, disk). The range of integrated galaxy colors is $1.2 < V - H < 3.3$, with a median color of $V - H = 2.6$. Most of the sample is comprised of disk galaxies and, as expected, the $V - H$ colors of the galaxy bulges are generally larger (redder) than the integrated colors of the entire galaxies by a median value of 0.75 mag.

4.3. Distances

To convert the observed magnitudes to luminosities, we estimated D_L based on the apparent redshifts of the galaxies. We conservatively adopted an uncertainty of 500 km s^{-1} in peculiar velocities for each distance estimate, based on the distribution of peculiar velocities derived by Tully et al. (2008). This works out to a 17% uncertainty at $z = 0.01$, and decreases as z increases. We caution that this uncertainty may still be significantly underestimated in the case of individual galaxies.

Four of the nearest galaxies in the sample have distances in the literature that were derived through other techniques. We summarize these distance measurements and their potential uncertainties in Bentz et al. (2013) but, in brief, they were generally retrieved from the Extragalactic Distance Database (Tully et al. 2009) and derived from an average of the distance moduli for galaxies within the same group. The exception is NGC 3227, where the distance measurement comes from an analysis of the surface brightness fluctuations of NGC 3226 (Tonry et al. 2001), with which it is interacting.

Adopted distances and their uncertainties are listed in Table 3.

4.4. Stellar Masses

We estimated the stellar M/L of each galaxy using the $V - H$ color and the relationships tabulated by Bell & de Jong (2001) in their Table 1. Following their work, we assume solar absolute magnitudes of $M_V = 4.82$ (Cox 2000) and $M_H = 3.37$ (Worthey 1994) and we derive the expected stellar mass in the

V and H passbands, which are identical and are listed as “ $\log M_{\text{stars}} \text{ (Bd01)}$ ” in Table 4. The uncertainties in the stellar masses are based on the propagated uncertainties in the photometry and the distances. The steeper dependency of M/L on bluer colors leads to uncertainties in the stellar masses that are roughly twice as large when based on the luminosity in V as for H . To be conservative, we adopt the larger uncertainties based on V .

We also estimated the stellar M/L of each galaxy using the relationships tabulated by Into & Portinari (2013), who used updated population synthesis models and applied prescriptions to more accurately account for thermally pulsing asymptotic giant branch stars, which can strongly affect near-infrared photometry of galaxies. We apply their “dusty” models (their Table 6) because we have not attempted to correct for dust internal to the galaxies, and the predominantly late types of the galaxies in our sample mean that they cannot be considered “dust free.” Adopting the solar absolute magnitudes of $M_V = 4.828$ and $M_H = 3.356$ derived by Into & Portinari (2013) for consistency, we determined the expected stellar masses in the V and H passbands. Unlike the masses estimated from the relationships of Bell & de Jong (2001), the two passbands do not predict exactly the same stellar masses, but the differences are only at the 1% level. We adopted the stellar masses based on the luminosity in V , again because their larger propagated uncertainties make them a more conservative choice, and we list these in Table 4 as “ $\log M_{\text{stars}} \text{ (IP13)}$.”

The stellar masses predicted by the relationships of Into & Portinari (2013) are typically a factor of 2.4 times smaller than those derived from the relationships tabulated by Bell & de Jong (2001), although for the smallest $V - H$ colors in the sample, they can disagree by a factor of ~ 4 – 5 . Some of this difference can be attributed to the choice of a “diet” Salpeter initial mass function (IMF) used by Bell & de Jong and a Kroupa IMF adopted by Into & Portinari. If we adjust the M/L prescription of Bell & de Jong by -0.15 dex to better match a Kroupa IMF (Bell et al. 2003), then the agreement is better, although the stellar masses predicted by the Into & Portinari M/L relations are still typically 1.7 times smaller than those predicted by Bell & de Jong. This difference agrees with the factor-of-two lighter masses found by Into & Portinari when comparing their new stellar population models with previous models, which they attribute to updates like their treatment of thermally pulsing asymptotic giant branch stars. Kormendy & Ho (2013) also find that the M/L ratios predicted by Into & Portinari are, on average, a factor of 1.34 smaller than those predicted by the dynamics of the galaxy, although it is unclear how much of the discrepancy may be attributed to dark matter. Given the uncertainties in the methods, we report the results using both the Bell & de Jong and the Into & Portinari prescriptions throughout this work.

4.5. Black Hole Masses

Black hole masses for all galaxies were drawn from the compilation of reverberation-based masses in the AGN Black Hole Mass Database (Bentz & Katz 2015). The basic technique of reverberation mapping (Blandford & McKee 1982; Peterson 1993) involves time-resolved spectrophotometry collected over a long time baseline and with dense time sampling (for nearby Seyferts, this typically amounts to daily sampling over a baseline of a few months). Variations in the continuum flux are

Table 4
Stellar and Black Hole Masses

Object	Bulge			Galaxy			
	$V - H$ (mag)	$\log M_{\text{stars}}$ (Bd01) (M_{\odot})	$\log M_{\text{stars}}$ (IP13) (M_{\odot})	$V - H$ (mag)	$\log M_{\text{stars}}$ (Bd01) (M_{\odot})	$\log M_{\text{stars}}$ (IP13) (M_{\odot})	$\log M_{\text{BH}}$ (M_{\odot})
Mrk 335	3.22	10.22 ± 0.23	9.99 ± 0.30	2.58	10.17 ± 0.23	9.78 ± 0.30	$7.230^{+0.042}_{-0.044}$
Mrk 1501	2.82	10.82 ± 0.23	10.49 ± 0.30	1.64	10.63 ± 0.23	10.00 ± 0.30	$8.067^{+0.119}_{-0.165}$
PG 0026+129	1.38	10.24 ± 0.23	9.55 ± 0.30	1.38	10.24 ± 0.23	9.55 ± 0.30	$8.487^{+0.096}_{-0.119}$
Mrk 590	3.19	10.42 ± 0.23	10.19 ± 0.30	3.16	11.25 ± 0.23	11.01 ± 0.30	$7.570^{+0.062}_{-0.074}$
3C 120	3.59	10.83 ± 0.23	10.70 ± 0.30	2.86	10.86 ± 0.23	10.54 ± 0.30	$7.745^{+0.038}_{-0.040}$
Akn 120	2.87	10.85 ± 0.23	10.53 ± 0.30	2.66	11.04 ± 0.23	10.68 ± 0.30	$8.068^{+0.048}_{-0.063}$
Mrk 6	3.67	10.93 ± 0.23	10.82 ± 0.30	2.62	10.68 ± 0.23	10.31 ± 0.30	$8.102^{+0.037}_{-0.041}$
Mrk 79	3.25	10.49 ± 0.23	10.27 ± 0.30	2.59	10.69 ± 0.23	10.31 ± 0.30	$7.612^{+0.107}_{-0.136}$
PG 0844+349	3.05	10.58 ± 0.23	10.31 ± 0.30	2.68	10.72 ± 0.23	10.36 ± 0.30	$7.858^{+0.154}_{-0.230}$
Mrk 110	4.12	10.64 ± 0.23	10.64 ± 0.30	3.27	10.68 ± 0.23	10.47 ± 0.30	$7.292^{+0.101}_{-0.097}$
NGC 3227	4.15	10.64 ± 0.23	10.65 ± 0.30	3.12	11.03 ± 0.23	10.78 ± 0.30	$6.775^{+0.084}_{-0.112}$
NGC 3516	3.18	10.53 ± 0.25	10.30 ± 0.32	2.37	10.52 ± 0.25	10.08 ± 0.32	$7.395^{+0.037}_{-0.061}$
SBS 1116+583A	3.00	9.33 ± 0.23	9.05 ± 0.30	2.79	10.38 ± 0.23	10.05 ± 0.30	$6.558^{+0.081}_{-0.088}$
Arp 151	3.27	10.40 ± 0.23	10.19 ± 0.30	3.14	10.44 ± 0.23	10.19 ± 0.30	$6.670^{+0.045}_{-0.054}$
Mrk 1310	3.12	9.96 ± 0.23	9.71 ± 0.30	2.34	9.98 ± 0.23	9.53 ± 0.30	$6.212^{+0.071}_{-0.089}$
NGC 4051	2.70	8.92 ± 0.25	8.56 ± 0.32	1.88	10.13 ± 0.25	9.56 ± 0.32	$6.130^{+0.121}_{-0.155}$
NGC 4151	3.36	9.78 ± 0.25	9.59 ± 0.32	2.59	10.40 ± 0.25	10.01 ± 0.32	$7.555^{+0.051}_{-0.047}$
Mrk 202	3.54	10.04 ± 0.23	9.90 ± 0.30	2.62	10.07 ± 0.23	9.69 ± 0.30	$6.133^{+0.166}_{-0.173}$
NGC 4253	3.43	9.81 ± 0.24	9.64 ± 0.31	2.20	10.18 ± 0.24	9.70 ± 0.31	$6.822^{+0.050}_{-0.057}$
PG 1226+023	1.20	11.11 ± 0.23	10.37 ± 0.30	1.20	11.11 ± 0.23	10.37 ± 0.30	$8.839^{+0.077}_{-0.113}$
PG 1229+204	2.99	11.06 ± 0.23	10.77 ± 0.30	2.76	11.07 ± 0.23	10.73 ± 0.30	$7.758^{+0.175}_{-0.219}$
NGC 4593	3.30	10.68 ± 0.25	10.48 ± 0.32	2.43	10.83 ± 0.25	10.40 ± 0.32	$6.882^{+0.084}_{-0.104}$
NGC 4748	3.60	10.79 ± 0.24	10.66 ± 0.30	2.57	10.46 ± 0.24	10.07 ± 0.30	$6.407^{+0.110}_{-0.183}$
PG 1307+085	1.89	11.11 ± 0.23	10.55 ± 0.30	1.89	11.11 ± 0.23	10.55 ± 0.30	$8.537^{+0.094}_{-0.161}$
Mrk 279	3.86	10.98 ± 0.23	10.92 ± 0.30	3.24	11.07 ± 0.23	10.86 ± 0.30	$7.435^{+0.099}_{-0.133}$
PG 1411+442	2.83	11.01 ± 0.23	10.69 ± 0.30	2.83	11.01 ± 0.23	10.69 ± 0.30	$8.539^{+0.125}_{-0.169}$
PG 1426+015	2.60	10.87 ± 0.23	10.48 ± 0.30	2.42	11.10 ± 0.23	10.67 ± 0.30	$9.007^{+0.106}_{-0.164}$
Mrk 817	4.38	10.84 ± 0.23	10.91 ± 0.30	2.76	10.97 ± 0.23	10.63 ± 0.30	$7.586^{+0.064}_{-0.072}$
PG 1613+658	2.77	11.68 ± 0.23	11.34 ± 0.30	2.77	11.68 ± 0.23	11.34 ± 0.30	$8.339^{+0.164}_{-0.271}$
PG 1617+175	1.87	10.31 ± 0.23	9.74 ± 0.30	1.87	10.31 ± 0.23	9.74 ± 0.30	$8.667^{+0.084}_{-0.128}$
PG 1700+518	1.95	11.23 ± 0.23	10.69 ± 0.30	1.95	11.23 ± 0.23	10.69 ± 0.30	$8.786^{+0.091}_{-0.103}$
3C 390.3	3.03	10.60 ± 0.23	10.33 ± 0.30	2.99	10.94 ± 0.23	10.66 ± 0.30	$8.638^{+0.040}_{-0.046}$
Zw 229-015	2.95	9.94 ± 0.23	9.64 ± 0.30	2.35	10.32 ± 0.23	9.87 ± 0.30	$6.913^{+0.075}_{-0.119}$
NGC 6814	3.27	9.67 ± 0.29	9.45 ± 0.35	2.17	10.34 ± 0.29	9.85 ± 0.35	$7.038^{+0.056}_{-0.058}$
Mrk 509	2.71	10.76 ± 0.23	10.40 ± 0.30	$8.049^{+0.035}_{-0.035}$
PG 2130+099	3.98	11.14 ± 0.23	11.11 ± 0.30	3.17	11.16 ± 0.23	10.92 ± 0.30	$7.433^{+0.055}_{-0.063}$
NGC 7469	3.32	9.84 ± 0.23	9.64 ± 0.30	2.42	10.88 ± 0.23	10.45 ± 0.30	$6.956^{+0.048}_{-0.050}$

“echoed” in the broad emission lines, and the time delay between the two is based on the light-travel time between the two regions where the signals arise, namely the accretion disk and the broad line region.

The black hole masses are determined as

$$M_{\text{BH}} = f \frac{c\tau V^2}{G}, \quad (2)$$

where $c\tau$ is the measured time delay for a broad emission line, V is the velocity width of that same emission line, and G is the gravitational constant. The factor f is an order-unity scaling factor that is necessary to account for the generally unknown geometry and detailed kinematics of the broad line region in the AGNs. The value of f ranges from 2.8 to 5.5 in the literature, with most current studies finding $f \approx 4$. We adopted the scaling factor of $\langle f \rangle = 4.3$ determined by Grier et al. (2013).

5. Discussion

With the measurements of luminosities and masses derived in the previous sections, we examine several black hole scaling relationships here. Linear regressions were carried out with a Bayesian approach using the LINMIX_ERR algorithm (Kelly 2007), which includes measurement errors in both coordinates and a component of intrinsic, random scatter. The values and uncertainties that we report for the slope, intercept, and scatter of each relationship are the median values and 1σ widths of a large number of draws from the posterior probability distribution for each term.

5.1. Black Hole Mass–Bulge Luminosity Relationship

The relationship between black hole mass and bulge luminosity, $M_{\text{BH}}-L_{\text{bulge}}$ was one of the first black hole scaling relationships to be discovered (Kormendy & Richstone 1995).

However, it was soon eclipsed by the $M_{\text{BH}}-\sigma_*$ relationship (Ferrarese & Merritt 2000; Gebhardt et al. 2000), which was initially reported to have a smaller intrinsic scatter and was therefore viewed as being the more fundamental scaling relationship. However, improvements in the black hole mass measurements, in particular, have led to much tighter $M_{\text{BH}}-L_{\text{bulge}}$ relationships in recent years where the reported scatter is similar to that of the $M_{\text{BH}}-\sigma_*$ relationship (Marconi & Hunt 2003; Gültekin et al. 2009). These studies have tended to focus on bulge-dominated galaxies while neglecting the late-type galaxies common among local Seyfert hosts.

A notable exception, however, is Wandel (2002), who drew photometry from the literature to investigate the $M_{\text{BH}}-L_{\text{bulge}}$ relationship for AGN host galaxies with black hole masses from reverberation mapping. A homogeneous reanalysis of the AGN black hole masses by Peterson et al. (2004) combined with consistent bulge photometry derived from high-quality *HST* imaging and galaxy photometric decompositions allowed Bentz et al. (2009b) to update the results of Wandel (2002), finding that $M_{\text{BH}}-L_{\text{bulge}}$ for disk-dominated active galaxies is similar in form and scatter to that of bulge-dominated galaxies with predominantly quiescent black holes and masses derived from dynamical modeling.

Here, we are able to improve upon the results of Bentz et al. (2009b) by extending the sample to lower black hole masses, increasing the number of galaxies included in the fit by 40%, and by examining the relationship in both the optical and the near-infrared. This last point is an important addition because it allows for the effects of dust and recent star formation on the photometry to be mitigated.

For each galaxy, we identified the photometric component most consistent with the expected properties of a bulge. In particular, we looked for a round ($0.7 \lesssim q \lesssim 1.0$) photometric component with Sérsic index $n > 1.0$ and $r < r_{\text{disk}}$. In one instance (Mrk 509), there was no such model component and so we do not include it here in the analysis of galaxy bulges. Mrk 509 is thus consistent with either a bulgeless disk galaxy or a disk galaxy with a compact bulge that we could not separate from the central AGN. Some of the PG quasars, on the other hand, were modeled by a single spheroidal component which we include as a “bulge” here. We do not attempt to discriminate between pseudobulges and classical bulges because we have limited kinematic information regarding the bulges of these galaxies. Numerous studies have shown that pseudobulge identification can be extremely uncertain when it is based solely on photometric information (e.g., Kormendy & Kennicutt 2004; Läscher et al. 2014). In the *V* band, we find the best-fit relationship between the black hole mass and bulge luminosity to be

$$\log \frac{M_{\text{BH}}}{M_{\odot}} = (0.84 \pm 0.10) \log \left(\frac{L_{V,\text{bulge}}}{10^{10} L_{\odot}} \right) + (7.71 \pm 0.08) \quad (3)$$

with a typical scatter of (0.23 ± 0.06) dex. This is similar to the slope found by Bentz et al. (2009b) using a smaller number of galaxies in the reverberation sample and covering a smaller range of black hole masses. The scatter is much decreased, however, from ~ 0.4 dex to 0.23 dex.

In the *H* band, we find a best-fit relationship of

$$\log \frac{M_{\text{BH}}}{M_{\odot}} = (1.05 \pm 0.14) \log \left(\frac{L_{H,\text{bulge}}}{10^{10} L_{\odot}} \right) + (7.06 \pm 0.11) \quad (4)$$

with a typical scatter of (0.25 ± 0.07) dex. Surprisingly, the scatter in the near-infrared relationship is statistically equivalent to that of the optical relationship, suggesting that dust and/or recent star formation are not strong contributors to the intrinsic scatter in the relationship. As previously mentioned, however, there is still room for improvement in the distances, so it is likely that the scatter in both the optical and near-infrared relationships could be further decreased in the future through efforts to determine distances that do not rely on the galaxy redshift.

We display these relationships in Figure 3. The solid line shows the best fit, while the gray shaded regions show the uncertainties in the fit. We denote broad-line Seyferts 1s (BLS1s) with filled circles and narrow-line Seyferts 1s (NLS1s) with open circles. We follow the original definition of Osterbrock & Pogge (1985) and select NLS1s in cases where the broad $H\beta$ emission line has $\text{FWHM} < 2000 \text{ km s}^{-1}$. While the NLS1s tend to be associated with lower-mass black holes in lower-luminosity bulges, they exhibit the same scatter and general scaling relationship as the BLS1s. Some studies of NLS1s with black hole estimates have shown them to be significantly undermassive relative to BLS1s (e.g., Mathur et al. 2012), but we see no strong tendency for NLS1s to be undermassive relative to the other reverberation-mapped AGNs included here.

Kormendy & Ho (2013) report a near-infrared $M_{\text{BH}}-L_{\text{bulge}}$ relationship in the 2MASS K_s band for quiescent galaxies that are ellipticals or contain classical bulges, and for which black hole masses have been determined through dynamical modeling. They find a slightly steeper slope of 1.21 and a scatter of 0.31 dex, both of which are consistent within the errors with our finding for the active galaxy sample in *H*. The slightly higher intercept for their sample compared to ours is increased by the color difference between the *H* and *K* bands, given that galaxies are typically somewhat brighter in *K* than *H*.

While Kormendy & Ho (2013) do not report a fit to the $M_{\text{BH}}-L_{\text{bulge}}$ relationship in *V*, they do tabulate bulge absolute magnitudes in *V*. We fit the *V*-band relationship matching their accepted sample and adopted uncertainties and find a slope that agrees with their value reported for the K_s band, which is steeper than the slope that we find in *V* for the active galaxy sample. The intercept is also somewhat higher, although the fit to their sample agrees with our findings for the active galaxy sample at the low-mass end. The fits to the Kormendy & Ho (2013) sample are shown as black dashed lines in Figure 3. It is important to note that the active and quiescent samples primarily probe different regions of parameter space in this plot: the active galaxy sample is heavily dominated by galaxies with $M_{\text{BH}} < 10^8 M_{\odot}$, while the vast majority of galaxies in the quiescent sample have $M_{\text{BH}} > 10^8 M_{\odot}$.

Läscher et al. (2016) report deep *H*-band imaging and surface brightness decompositions for a sample of nine megamaser galaxies with accurate black hole masses. We find that the megamasers are contained wholly within the scatter of the active galaxy sample presented here in the *H* band. With the good agreement between the active galaxies, the megamasers, and the

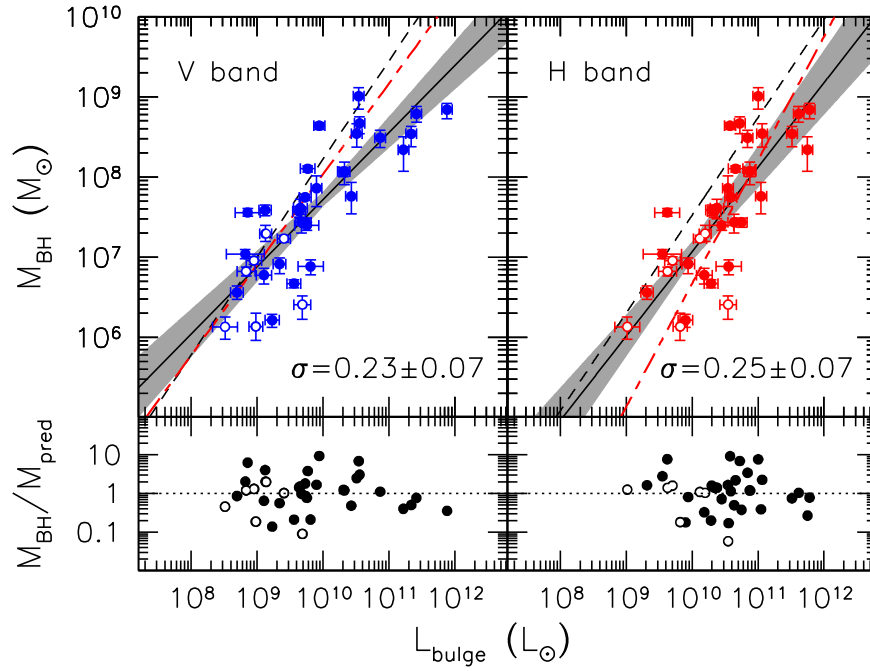


Figure 3. Black hole mass as a function of the bulge luminosity of the galaxy, as determined from *V*-band photometry (left) and *H*-band photometry (right). The solid lines show the best fits, while the gray shaded regions show the 1σ uncertainties on the fits. The scatter for the *V*-band relationship is formally smaller than that for the *H*-band relationship, but they are equivalent within the uncertainties. The filled symbols denote the broad-line Seyfert 1s while the open symbols denote narrow-line Seyfert 1s, which appear to follow the same relationship and scatter. The black dashed lines show the best fits to the quiescent galaxy sample of Kormendy & Ho (2013), while the red long-short dashed lines show the best fits to the combined samples, including the *H*-band measurements of megamasers from Läscher et al. (2016). The bottom panels show the distributions of measured M_{BH} relative to M_{BH} predicted by the best fit, as a function of L_{bulge} .

quiescent galaxy sample, we therefore refit the $M_{\text{BH}}-L_{\text{bulge}}$ relationship in *H* with all three samples combined. Based on the typical galaxy properties in 2MASS reported by Jarrett (2000), we adopt $\langle H - K_s \rangle = 0.3$ mag for the quiescent sample, which should account for any average color offset between the two filters (although we note that the scatter in $H - K_s$ values is typically ~ 0.2 mag, even for galaxies with a specific morphological type). The best fit is

$$\log \frac{M_{\text{BH}}}{M_{\odot}} = (1.31 \pm 0.09) \log \left(\frac{L_{H,\text{bulge}}}{10^{10} L_{\odot}} \right) + (7.27 \pm 0.08) \quad (5)$$

with a typical scatter of 0.26 ± 0.05 dex. While Läscher et al. (2016) do not report *V*-band measurements for the megamaser sample, we can investigate the $M_{\text{BH}}-L_{\text{bulge}}$ relationship in *V* for the active and quiescent samples combined. When we do, we find a best fit of

$$\log \frac{M_{\text{BH}}}{M_{\odot}} = (1.13 \pm 0.08) \log \left(\frac{L_{V,\text{bulge}}}{10^{10} L_{\odot}} \right) + (8.04 \pm 0.06) \quad (6)$$

with a typical scatter of (0.24 ± 0.05) dex. These fits are displayed as the red long-dashed lines in Figure 3. In both the *H* and *V* bands, the best fit for the combined sample has an almost identical scatter to that found for the active sample alone, even though the combination of the samples more than doubles the number of points being fit and extends the range of M_{BH} by an order of magnitude. This may indicate that the

galaxies in all three samples are drawn from the same parent population.

5.2. Black Hole Mass–Galaxy Luminosity Relationship

We also examined the relationship between black hole mass and total luminosity of the host galaxy. We find a clear correlation between these two measurements, in both the optical and the near-infrared. The best-fit relationships are found to be

$$\log \frac{M_{\text{BH}}}{M_{\odot}} = (1.25 \pm 0.22) \log \left(\frac{L_{V,\text{galaxy}}}{10^{11} L_{\odot}} \right) + (8.26 \pm 0.16) \quad (7)$$

in the *V* band, with a typical scatter of (0.34 ± 0.09) dex, and

$$\log \frac{M_{\text{BH}}}{M_{\odot}} = (1.56 \pm 0.24) \log \left(\frac{L_{H,\text{galaxy}}}{10^{11} L_{\odot}} \right) + (7.75 \pm 0.10) \quad (8)$$

in the *H* band, with a typical scatter of (0.32 ± 0.09) dex.

While the scatter is somewhat higher than that of the $M_{\text{BH}}-L_{\text{bulge}}$ relationship, the fact that there is still a relatively tight relationship found when the total galaxy luminosity is used (see Figure 4) suggests that bulge/disk decompositions can be avoided when estimating black hole masses from broadband photometry of disk galaxies, but with a loss of some accuracy. This may be of particular interest for large photometric surveys that are operational or coming online soon (e.g., LSST), where automated measurements will be key to making sense of the large data sets that will be produced.

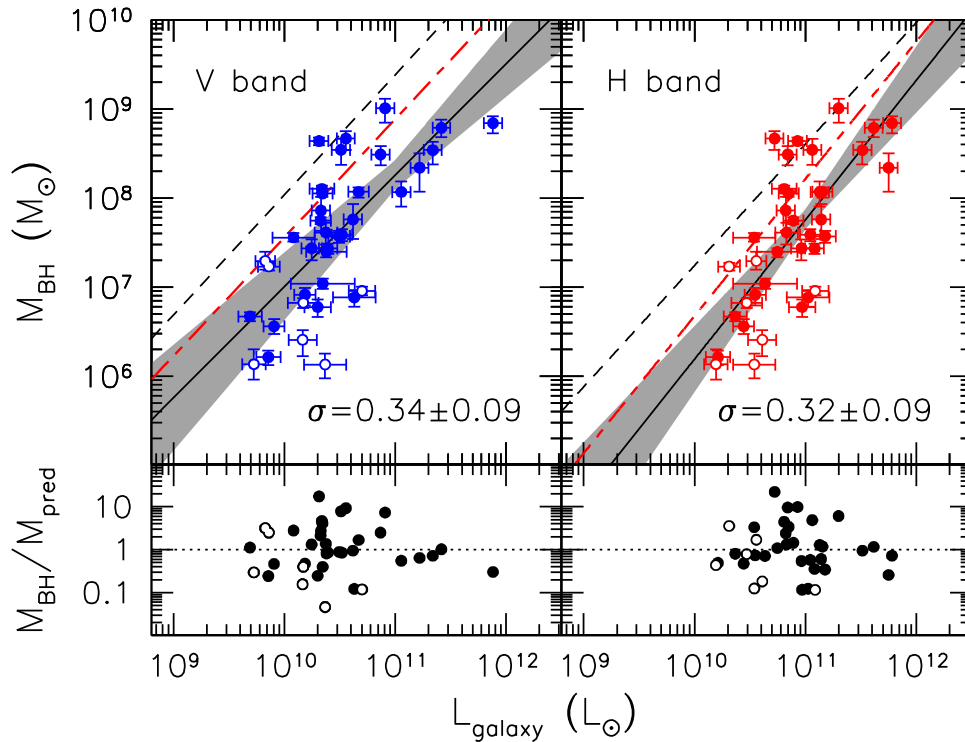


Figure 4. Black hole mass as a function of the total luminosity of the galaxy, as determined from *V*-band photometry (left) and *H*-band photometry (right). The solid lines show the best fits, while the gray shaded regions show the 1σ uncertainties on the fits. The scatter for the *H*-band relationship is formally smaller than that for the *V*-band relationship, but they are equivalent within the uncertainties. The black dashed lines show the best fits to the quiescent galaxy sample of Kormendy & Ho (2013), while the red long-short dashed lines show the best fits to the combined samples, including the *H*-band measurements of megamasers from Läsker et al. (2016). The bottom panels show the distributions of measured M_{BH} relative to M_{BH} predicted by the best fit, as a function of L_{galaxy} .

Our best-fit relationships for active galaxies may again be compared to the Kormendy & Ho (2013) sample of quiescent galaxies. The best-fit relationships based on their tabulated measurements in *V* and *K_s* have similar slopes and scatter to our findings, but their intercepts are significantly higher. This appears to stem from the differences in morphology between their sample and ours, as well as the different ranges of M_{BH} between the two samples. While the intercepts for the $M_{\text{BH}}-L_{\text{bulge}}$ relationships traced by the active galaxy sample show good agreement with the quiescent galaxies, two-thirds of the galaxies in the Kormendy & Ho (2013) sample are ellipticals. Thus, the $M_{\text{BH}}-L_{\text{galaxy}}$ relationships for their sample are very similar to the $M_{\text{BH}}-L_{\text{bulge}}$ relationships, because two-thirds of the points between them are exactly the same. On the other hand, the active galaxy sample is dominated by later-type galaxies where the bulge contributes a smaller fraction of the integrated galaxy light, and so the best-fit $M_{\text{BH}}-L_{\text{bulge}}$ and $M_{\text{BH}}-L_{\text{galaxy}}$ relationships that we find for the active galaxies are quite different from each other.

We looked at the bulge-to-total ratios for the active galaxy sample and investigated whether splitting the sample into “early” ($B/T > 0.5$) and “late” ($B/T < 0.5$) types uncovered any offsets or separations among the sample that may lead to better agreement with the quiescent galaxy sample. The only obvious difference between these two subsamples is that the “early” types have more massive black holes than the “late” types, and so a cut in B/T is similar to a cut in M_{BH} and does not improve the agreement. As before, we also investigated the location of the Läsker et al. (2016) megamasers and find that they are wholly contained within the *H*-band scatter of the active galaxy sample. If we again combine the active,

quiescent, and megamaser samples as before, we find best fits of

$$\log \frac{M_{\text{BH}}}{M_{\odot}} = (1.33 \pm 0.17) \log \left(\frac{L_{V,\text{galaxy}}}{10^{11} L_{\odot}} \right) + (8.89 \pm 0.13) \quad (9)$$

in the *V* band, with a typical scatter of (0.55 ± 0.09) dex, and

$$\log \frac{M_{\text{BH}}}{M_{\odot}} = (1.54 \pm 0.18) \log \left(\frac{L_{H,\text{galaxy}}}{10^{11} L_{\odot}} \right) + (8.22 \pm 0.08) \quad (10)$$

in the *H* band, with a typical scatter of (0.52 ± 0.08) dex. Thus, while the scatter is significantly increased when galaxies of all morphological types are treated equally, it is likely more representative of the true uncertainty on black hole mass estimates from the total galaxy luminosity.

5.3. Black Hole Mass–Bulge Stellar Mass Relationship

The relationship between black hole mass and bulge stellar mass is expected to be the physical basis for the $M_{\text{BH}}-L_{\text{bulge}}$ relationship, where bulge light traces mass. A variety of methods have been used to investigate this relationship in the past, often with the aim of decoupling the $M_{\text{BH}}-M_{\text{bulge}}$ relationship from any dependence on the $M_{\text{BH}}-L_{\text{bulge}}$ relationship so they can be studied independently.

For example, Magorrian et al. (1998) carried out axisymmetric dynamical models to constrain the bulge mass and the black hole mass simultaneously. Marconi & Hunt (2003) measured effective bulge radii from 2MASS imaging for

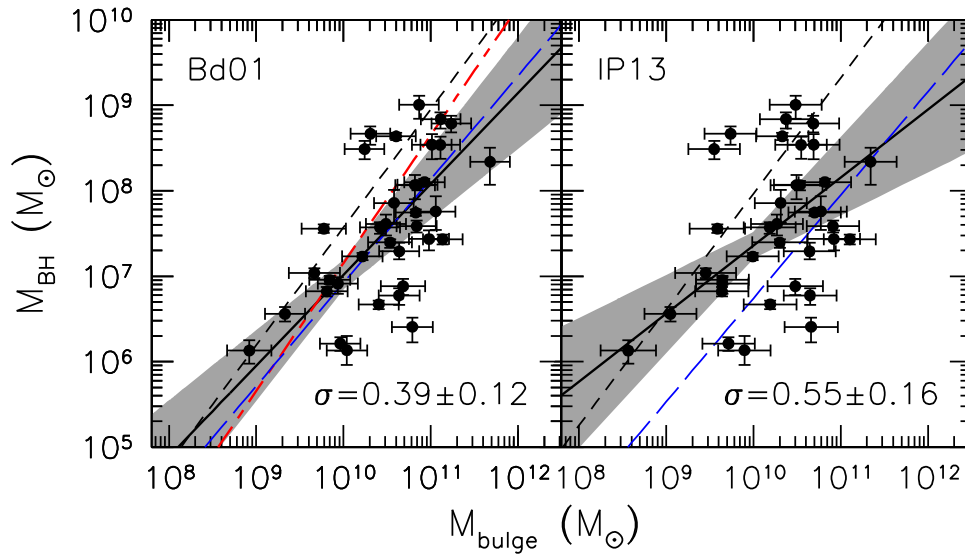


Figure 5. Black hole mass as a function of the bulge stellar mass, where the stellar mass is calculated based on the $V - H$ color and the M/L prescriptions of Bell & de Jong (2001) (left) and Into & Portinari (2013) (right). The solid lines and gray regions show the best-fit lines and 1σ uncertainties on the fits. The dashed lines show the best fit for the sample of quiescent galaxies tabulated by Kormendy & Ho (2013). The blue long-dashed lines show the best fit determined by Sijacki et al. (2015) for galaxies from the Illustris simulation. The red long-short dashed line is the best fit when the active galaxies, quiescent galaxies, and megamaser samples are combined.

quiescent galaxies with dynamical black hole masses. The bulge radii were combined with σ_* to predict M_{bulge} under the assumption that bulges behave similarly to isothermal spheres. Häring & Rix (2004), on the other hand, numerically solved the spherical Jeans equation while matching published luminosity and σ_* profiles for quiescent galaxies with dynamical black hole masses.

We can examine this relationship for active galaxies by estimating the bulge stellar mass from its optical–near-infrared color and the M/L prescriptions described above. The best-fit relationship between the black hole mass and the stellar mass of the bulge, based on the Bell & de Jong (2001) M/L predictions, is found to be

$$\log \frac{M_{\text{BH}}}{M_{\odot}} = (1.06 \pm 0.24) \log \left(\frac{M_{\text{bulge}}}{10^{10} M_{\odot}} \right) + (7.02 \pm 0.17) \quad (11)$$

with a typical scatter of (0.39 ± 0.12) dex.

If we estimate M/L using the prescriptions of Into & Portinari (2013), we find the best fit to be

$$\log \frac{M_{\text{BH}}}{M_{\odot}} = (0.80 \pm 0.30) \log \left(\frac{M_{\text{bulge}}}{10^{10} M_{\odot}} \right) + (7.36 \pm 0.15) \quad (12)$$

with a typical scatter of (0.55 ± 0.16) dex. These relationships are displayed in Figure 5.

For a direct comparison with the quiescent galaxy sample, we recalculated the bulge masses based on the absolute V magnitudes of the bulges and the $V - K_s$ colors tabulated by Kormendy & Ho (2013) with the M/L prescriptions of both Bell & de Jong (2001) and Into & Portinari (2013). Because Kormendy & Ho (2013) only provide an integrated $V - K_s$ color for each galaxy, we note that we would expect there to be a bias in the bulge masses derived for the disk galaxies in their sample because of the different colors of bulges and disks. The best-fit relationships for the quiescent galaxies are shown as the black dashed lines in Figure 5.

While the active galaxy sample displays a linear relationship between M_{BH} and bulge stellar mass, the quiescent galaxy relationships are considerably steeper. The two samples agree better using the M/L prescriptions of Bell & de Jong (2001), although both prescriptions show agreement between the samples at the low-mass end.

The megamaser sample of Läscher et al. (2016) reports M_{bulge} based on near-infrared *HST* and ground-based imaging and the M/L prescriptions of Bell et al. (2003), which allows for a simple comparison with our results. We again find that all nine megamasers are contained wholly within the scatter of the active galaxy sample, with no apparent offsets in bulge mass or black hole mass.

Noting that there is good agreement between the active, quiescent, and megamaser samples, we also fit the $M_{\text{BH}} - M_{\text{bulge}}$ relationship with all three samples combined. Assuming the Bell & de Jong (2001) M/L prescriptions, the best-fit relationship is

$$\log \frac{M_{\text{BH}}}{M_{\odot}} = (1.50 \pm 0.13) \log \left(\frac{M_{\text{bulge}}}{10^{10} M_{\odot}} \right) + (7.16 \pm 0.11) \quad (13)$$

with a scatter of (0.27 ± 0.06) dex. The red long-short dashed line in the left panel of Figure 5 displays this fit. While the slope is considerably steeper than that found for the active galaxy sample, they only disagree at the $\sim 1\sigma$ level. Furthermore, there is good agreement with the gray shaded region (which denotes the uncertainty on the fit to the active sample alone) over the range sampled by the active galaxies. This appears to indicate that all three samples may be drawn from the same parent population of galaxies.

We also compared our results to those of simulated galaxies. Some caution must be taken when interpreting such comparisons, because cosmological galaxy simulations are generally tuned to match a set of observables. For example, the slope of the $M_{\text{BH}} - M_{\text{bulge}}$ relationship is not expected to be affected by such tuning, but the intercept is. Furthermore, there is no

agreement on the best way to separate the bulges of late-type galaxies from their disks in simulations, where the resolution is often a limiting factor, so the simulated galaxies are either compared to samples of massive early-type galaxies where $M_{\text{bulge}} \approx M_{\text{galaxy}}$ (e.g., Schaye et al. 2015; Steinborn et al. 2015) or a prescription is applied to estimate the bulge contribution.

Sijacki et al. (2015) used the high-resolution hydrodynamical Illustris simulations to explore the predicted $M_{\text{BH}}-M_{\text{bulge}}$ relationship for galaxies. The total stellar mass within the stellar half-mass-radius was used as a proxy for the bulge mass. This simplification does not take into account different bulge mass fractions of galaxies, nor the fact that some galaxies may not have a bulge at all. Additionally, the Illustris simulations assumed a Chabrier IMF, which can be compared to a “diet” Salpeter like that employed by Bell & de Jong (2001) by adding 0.093 dex (Gallazzi et al. 2008). To compare with a Kroupa IMF like that employed by Into & Portinari (2013), on the other hand, we subtracted 0.057 dex (Bell et al. 2003; Herrmann et al. 2016). The best-fit relationship of Sijacki et al. (2015), with the IMF scaled appropriately, is displayed as the blue long-dashed lines in Figure 5. With a reported slope of 1.21, it is in good agreement with our findings, especially when we adopt the Bell & de Jong (2001) M/L prescriptions.

The large-volume Horizon-AGN simulations, which adopt a Salpeter IMF, were analyzed by Volonteri et al. (2016). To separate the bulge contribution, they tried various prescriptions, including examining the kinematics and also adopting a double Sérsic model for each galaxy, where the indices for the two Sérsic profiles were chosen to be [1.0, 1.0], [1.0, 4.0], or [1.0, 1.0 or 4.0]. The slope of the relationship based on these various prescriptions ranges from 0.75 to 1.05, which is in good agreement with our findings for the active galaxies using either the Bell & de Jong (2001) or Into & Portinari (2013) M/L prescriptions, although it is somewhat in tension with our results for the combined active, quiescent, and megamaser samples. This tension may result from incompleteness in the Horizon-AGN simulation for black holes with $M_{\text{BH}} \lesssim 2 \times 10^7 M_{\odot}$, which is the region probed by many of the active galaxies.

5.4. Black Hole Mass–Galaxy Stellar Mass Relationship

In the same way, we can examine the best-fit relationship between the black hole mass and the total stellar mass of the galaxy. When we adopt the Bell & de Jong (2001) M/L predictions, we find a best fit of

$$\log \frac{M_{\text{BH}}}{M_{\odot}} = (1.69 \pm 0.46) \log \left(\frac{M_{\text{stars}}}{10^{11} M_{\odot}} \right) + (8.05 \pm 0.18) \quad (14)$$

with a typical scatter of (0.38 ± 0.13) dex.

If we instead estimate M/L using the prescriptions of Into & Portinari (2013), we find the best fit to be

$$\log \frac{M_{\text{BH}}}{M_{\odot}} = (1.34 \pm 0.55) \log \left(\frac{M_{\text{stars}}}{10^{11} M_{\odot}} \right) + (8.49 \pm 0.41) \quad (15)$$

with a typical scatter of (0.49 ± 0.17) dex. These relationships are displayed in Figure 6.

Interestingly, the $M_{\text{BH}}-M_{\text{stars}}$ relationship based on the Into & Portinari (2013) M/L values is similar to that found by Reines & Volonteri (2015) for inactive black holes residing in ellipticals and classical bulges. This would seem to contradict their finding that active galaxies lie below the relationship defined by local quiescent galaxies, although a direct comparison is somewhat difficult given that they used M/L prescriptions of Zibetti et al. (2009), who employ a different initial mass function than Into & Portinari (2013).

We therefore recalculated the $M_{\text{BH}}-M_{\text{stars}}$ relationship for local quiescent galaxies based on the absolute V magnitudes and the $V - K_s$ colors tabulated by Kormendy & Ho (2013), using both the Bell & de Jong (2001) and Into & Portinari (2013) M/L prescriptions for direct comparison with the active galaxies in our sample. The best fits are shown as the dashed lines in Figure 6. Using the Bell & de Jong prescription, we find a nearly identical slope for the quiescent galaxies compared to the active galaxies, but an intercept that is 0.75 dex higher, supporting the findings of Reines & Volonteri (2015) that active galaxies fall below quiescent galaxies in this parameter space. However, using the Into & Portinari prescription instead, we find a slightly steeper slope for the quiescent galaxies which, when coupled with the intercept, show the two samples to be in general agreement at the low-mass end while diverging at the high-mass end.

If we again combine the active sample with the quiescent galaxies and the megamasers, we find a best-fit relationship of

$$\log \frac{M_{\text{BH}}}{M_{\odot}} = (1.84 \pm 0.25) \log \left(\frac{M_{\text{stars}}}{10^{11} M_{\odot}} \right) + (8.40 \pm 0.09) \quad (16)$$

with a scatter of (0.44 ± 0.10) dex. This fit is denoted with the red long-short dashed line in the left panel of Figure 6. Once again, the consistency with the results derived solely from the active galaxies seems to indicate that all of these subsamples may be drawn from the same parent population.

Recently, Shankar et al. (2016) investigated the potential for selection bias among the quiescent galaxy sample using Monte Carlo simulations and a large sample of galaxies drawn from the Sloan Digital Sky Survey. They concluded that the quiescent galaxy sample is selected from an upper “ridgeline” in the distribution of normal galaxy properties, leading to a bias of a factor of ~ 3 in the normalization of the $M_{\text{BH}}-\sigma_*$ relationship. If such a bias exists, that would argue against our choice of scaling factor for reverberation-based masses in the active galaxy sample, and would instead argue for $f \approx 1$. Interestingly, when we adopt $f = 1$ for the scaling of reverberation-based M_{BH} , and examine the $M_{\text{BH}}-M_{\text{stars}}$ relationship based on the M/L prescriptions of Bell & de Jong (2001), we find that the active galaxy sample closely follows the predicted unbiased relationship in Equation (6) of Shankar et al. (2016). The stellar masses predicted by Into & Portinari (2013), however, are undermassive compared to the predicted relationship, even when accounting for the slight differences in assumed IMF. However, it appears that bars will affect the measurements of effective radii (Meert et al. 2015) and possibly velocity dispersion (Batiste et al. 2017) that are adopted for the “unbiased” SDSS sample considered by Shankar et al. (2016). These effects will be strongest at the low-mass end, where most of the active galaxies in our sample are found, thus complicating the interpretation for

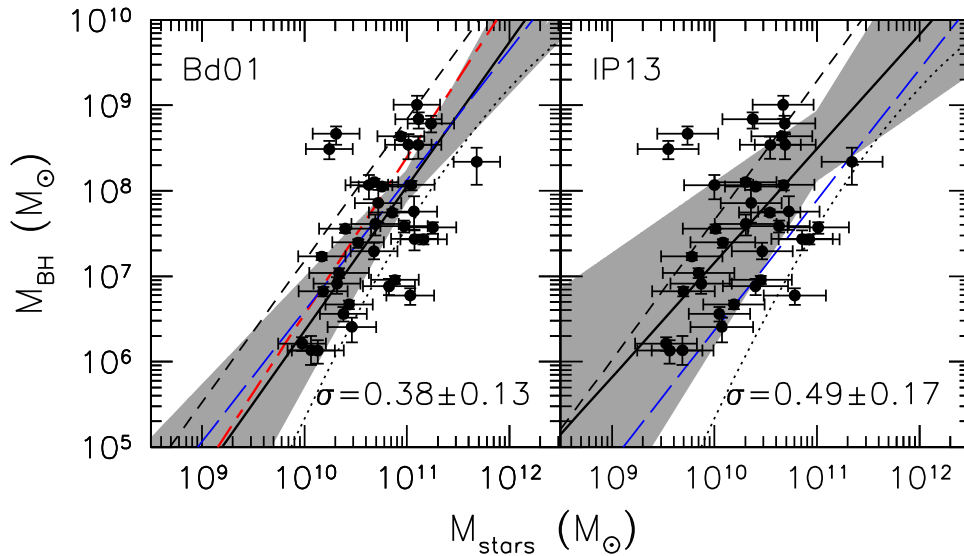


Figure 6. Black hole mass as a function of the total stellar mass of the galaxy, where the stellar mass is calculated based on the $V - H$ color and the M/L prescriptions of Bell & de Jong (2001) (left) and Into & Portinari (2013) (right). The solid lines and gray regions show the best-fit lines and 1σ uncertainties on the fits. The Bell & de Jong (2001) M/L prescriptions lead to a tighter relationship with a somewhat steeper slope. The dashed lines show the best fit for the sample of quiescent galaxies tabulated by Kormendy & Ho (2013). The dotted line is the predicted “unbiased” relationship of Shankar et al. (2016), which agrees extremely well with our measurements if we adopt M/L from Bell & de Jong (2001) and $f = 1$ rather than $f = 4.3$ for M_{BH} (as Shankar et al. 2016 recommend). The blue long-dashed lines show the relationship found for disk galaxies in the Illustris simulation (Mutlu-Pakdil et al. 2018), which agrees extremely well with our measurements of M_{BH} and M_{stars} when the M/L prescriptions of Bell & de Jong (2001) are adopted. The red long-short dashed line is the best fit when the active galaxies, quiescent galaxies, and megamaser samples are combined.

reverberation-based masses. Furthermore, forward modeling of velocity-resolved reverberation signals by Pancoast et al. (2014) and Grier et al. (2017) has constrained the geometry and kinematics of the broad line region and the black hole mass for nine AGNs, independent of any f factor. Both studies recover modeling-based black hole masses that agree well with M_{BH} values derived from traditional reverberation analysis and the use of $f \approx 4$ (as described in Section 4.5). These findings argue against the use of $f = 1$ for the proper scaling of reverberation masses, but do not rule out that there may be biases present in the quiescent galaxy sample.

Unlike for the $M_{\text{BH}}-M_{\text{bulge}}$ relationship, comparisons with simulated galaxies are much simpler when the entire galaxy stellar mass is used because the issues with bulge–disk decompositions are avoided, although the caveats related to the tuning of parameters in the simulations remain. Mutlu-Pakdil et al. (2018) recently examined the relationships between black holes and large-scale galaxy properties for $z = 0$ spiral galaxies in the Illustris simulations. Using the same IMF corrections described in the previous section, we compare our best-fit $M_{\text{BH}}-M_{\text{stars}}$ relationships to theirs (blue long-dashed lines in Figure 6) and we find excellent agreement, especially when we adopt the Bell & de Jong (2001) M/L prescriptions, which may argue against any potential bias in the reverberation-based M_{BH} scaling. Volonteri et al. (2016) examined the $M_{\text{BH}}-M_{\text{stars}}$ relationship for galaxies from the Horizon-AGN simulation, and found a slope that is somewhat shallower than we have found, although the low-mass end of their relationship may be biased by incompleteness. Steinborn et al. (2015) used the Magneticum Pathfinder Simulations to examine the $M_{\text{BH}}-M_{\text{stars}}$ relationship, excluding simulated galaxies for which $M_{\text{BH}} < 5 \times 10^7 M_{\odot}$. Perhaps unsurprisingly, their reported best-fit relationship (with a slope of 1.09) agrees with the most massive black holes in the active galaxy

sample ($M_{\text{BH}} \gtrsim 10^8 M_{\odot}$), but diverges at lower black hole masses, predicting a larger M_{BH} at fixed M_{stars} , similar to the findings of Volonteri et al. (2016).

Many large photometric surveys that are currently in operation or are upcoming will collect photometry in multiple filters. Considering that these surveys may need to be treated in an automated fashion, the stellar mass of the galaxy based on its color appears to be a better predictor of black hole mass than the total galaxy luminosity in a single filter. This can be seen from the decreased scatter in the $M_{\text{BH}}-M_{\text{stars}}$ relationship for the combined active, quiescent, and megamaser samples (0.44 ± 0.10 dex) relative to the $M_{\text{BH}}-L_{\text{galaxy}}$ relationship ($\sim 0.53 \pm 0.09$ dex).

5.5. Black Hole Mass Fraction

Finally, we investigated the typical fraction of black hole mass to stellar mass for each galaxy. We find a median value of $M_{\text{BH}}/M_{\text{stars}} = 0.0005 \pm 0.0049$; however, we also find a very clear relationship between $M_{\text{BH}}/M_{\text{stars}}$ and M_{BH} , while there appears to be no obvious relationship between $M_{\text{BH}}/M_{\text{stars}}$ and M_{stars} (see Figure 7).

For comparison, we derived the black hole mass fractions for the quiescent galaxy sample of Kormendy & Ho (2013) and found a median value of $M_{\text{BH}}/M_{\text{stars}} = 0.0058 \pm 0.0077$. At first glance, this would appear to demonstrate that active galaxies host undermassive black holes compared to quiescent galaxies. However, the samples cover different M_{BH} ranges, with the active galaxy sample skewed toward lower M_{BH} , while the quiescent galaxy sample is skewed to higher M_{BH} (see Figure 8), and $M_{\text{BH}}/M_{\text{stars}}$ seems to depend strongly on M_{BH} . For a better comparison between the two samples, we binned the galaxies in each sample by M_{BH} with bins of width 0.5 dex. For each bin with three or more objects, we computed the median black hole mass to stellar mass fraction. Figure 8 shows the median $M_{\text{BH}}/M_{\text{stars}}$ as a function of M_{BH} for the two

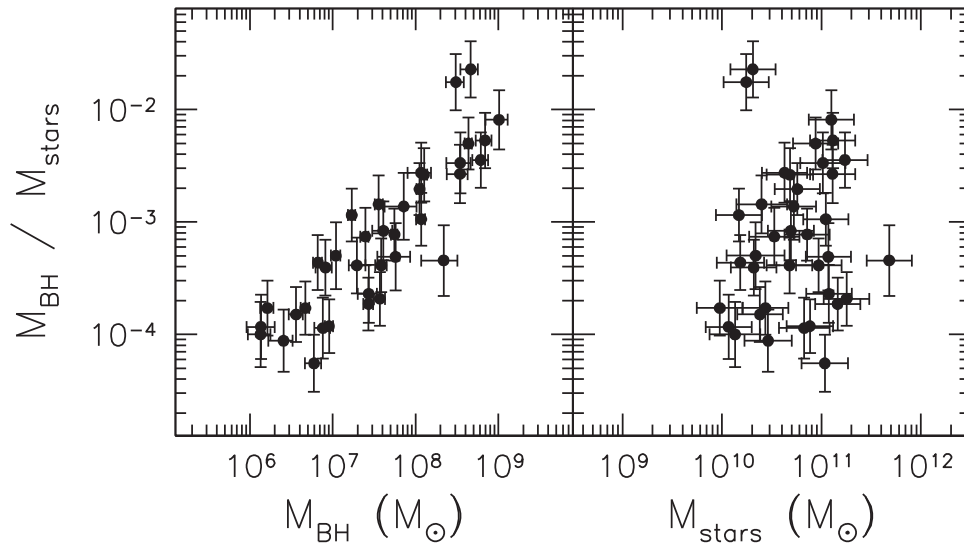


Figure 7. Black hole mass fraction as a function of black hole mass (left) and as a function of galaxy stellar mass (right). There is no correlation seen between black hole mass fraction and galaxy stellar mass, but there appears to be a strong correlation between black hole mass fraction and black hole mass, with more massive black holes commanding a larger mass fraction.

samples, with the active sample in red and the quiescent sample in black. The majority of the overlap between the samples exists within the range $10^7 < M_{\text{BH}}/M_{\odot} < 10^9$, with the range extending to lower black hole masses in the active galaxy sample, and extending to higher black hole masses in the quiescent galaxy sample. We have adopted M_{stars} based on the M/L predictions of Bell & de Jong (2001) in Figure 8 but, while the values slightly change, the overall trend is the same if we adopt M_{stars} based on the Into & Portinari (2013) M/L values. The two samples show broad agreement, both in the overall trend—with more massive black holes comprising larger mass fractions of their galaxies—and with the typical values for the black hole mass fraction at a fixed value of M_{BH} . While there seems to be a tendency for the active galaxies to lie slightly below the quiescent galaxies in the expected black hole mass fraction at a fixed black hole mass, the values agree within the standard deviation for each bin, and the small and uneven number of objects in each bin make it difficult to draw firm conclusions about any apparent offset between the two samples. Notably, the trend appears to continue across the full range of black hole masses probed by either sample.

We also examined the megamaser sample of Läscher et al. (2016) for comparison. Adopting the same bins for the megamaser sample as for the above two samples, we show the median $M_{\text{BH}}/M_{\text{stars}}$ in blue in Figure 8. There is no apparent offset between the megamaser and the reverberation samples, nor with the extension of the quiescent sample to lower black hole masses. Läscher et al. (2016) noted in their study that the megamaser galaxies appeared to probe a lower M_{BH} at fixed galaxy mass than the reverberation sample (as reported by Bentz et al. 2009a), but this discrepancy has been completely erased with the larger sample and extended range of M_{BH} and galaxy properties presented here.

The scaling of $M_{\text{BH}}/M_{\text{stars}}$ as a function of M_{BH} was previously noticed by Trakhtenbrot & Netzer (2010). Using large samples of local non-AGN galaxies and AGN galaxies at $z \approx 0.15, 1, 2$ and scaling relationships to predict M_{stars} and M_{BH} , they found that $M_{\text{BH}}/M_{\text{stars}} \propto (0.7 \pm 0.1)M_{\text{BH}}$. A formal fit to the active, quiescent, and maser galaxies examined

here finds

$$\log \frac{M_{\text{BH}}}{M_{\text{stars}}} = (0.71 \pm 0.04) \log \left(\frac{M_{\text{BH}}}{10^8 M_{\odot}} \right) - (2.80 \pm 0.04) \quad (17)$$

with a typical scatter of (0.04 ± 0.02) dex, which agrees well with a formal fit to the active galaxies alone, and to the estimated slope reported by Trakhtenbrot & Netzer (2010).

Interestingly, we find the same scaling between $M_{\text{BH}}/M_{\text{stars}}$ and M_{BH} among simulated galaxies from Illustris. Vogelsberger et al. (2014) provide black hole masses and galaxy stellar masses for two subsamples of representative “red” and “blue” galaxies from the Illustris simulation. The “blue” galaxies preferentially occupy the lower M_{BH} range that is probed here by the active and megamaser samples, and the “red” galaxies preferentially occupy the upper M_{BH} range probed by the quiescent galaxies. The scaling in $M_{\text{BH}}/M_{\text{stars}}$ as a function of M_{BH} in the simulated galaxies matches the observed galaxies extremely well in both slope and offset.

It is clear from these studies that the commonly used assumption of a constant $M_{\text{BH}}/M_{\text{stars}}$ is incorrect in the local universe and possibly up to $z \approx 2$. Attempts to search for cosmic evolution of black holes and host galaxies, or to search for differences in the evolutionary paths of distinct galaxy samples, should be careful to account for this scaling when the samples are not matched in M_{BH} .

We suggest that the physical meaning of this scaling may be related to differences in feedback efficiency as a function of galaxy mass. High-resolution and zoom-in simulations of individual galaxies show that supernova feedback is extremely effective at prohibiting black hole growth at early times (e.g., Dubois et al. 2015; Anglés-Alcázar et al. 2017; Trebitsch et al. 2018). Once the host galaxy reaches a critical mass ($M_{\text{stars}} \approx 10^9$ – $10^{10} M_{\odot}$; Dubois et al. 2015; Anglés-Alcázar et al. 2017), supernova feedback can no longer restrict the gas flow to the nucleus and the black hole will undergo a period of rapid growth, effectively “catching up” with the galaxy. This

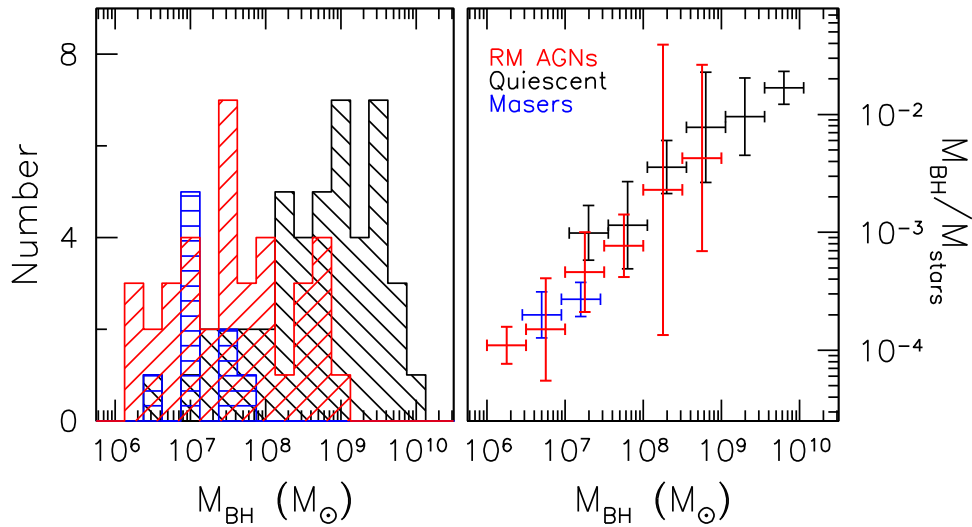


Figure 8. Left: histogram of black hole masses from the active sample (red), the quiescent sample (black), and the megamaser sample (blue). The majority of the overlap for the active and quiescent samples occurs at $10^7 \leq M_{\text{BH}}/M_{\odot} \leq 10^9$, while the megamasers are completely contained within the range of black hole masses probed by the active sample. Right: median black hole mass fraction as a function of black hole mass for the active sample (red), the quiescent sample (black), and the megamaser sample (blue). At least three objects contribute to each of the bins. The error bars show the standard deviation for the galaxies in the bin, while the error bars on black hole mass show the bin size. The bins for the quiescent galaxy sample and the megamaser sample have been slightly offset in M_{BH} for clarity.

period of rapid growth is short-lived, however, because AGN feedback soon becomes important and the black hole then regulates its own growth and the continued growth of the galaxy (e.g., Dubois et al. 2015; McAlpine et al. 2017). In this scenario, we may currently be witnessing the rapid growth phase for low-mass black holes in the local universe.

6. Summary

Using high-resolution optical *HST* images and deep, ground-based near-infrared images, we have constrained the photometric properties of 37 active galaxies hosting black holes with reverberation-based M_{BH} measurements. We have compared our results with those of megamaser galaxies and of quiescent galaxies with black hole masses from dynamical modeling, and we have re-examined several black hole–galaxy scaling relationships. In general, we find that megamasers behave as a subset of the active galaxy sample, and there is evidence that the active and megamaser samples may be drawn from the same parent population as the quiescent galaxies. We also find the following:

1. The $M_{\text{BH}}-L_{\text{bulge}}$ relationship for active galaxies is slightly steeper in the near-infrared than the optical, and both bandpasses exhibit similar scatter. There is general agreement between our results and those found for quiescent galaxies by Kormendy & Ho (2013) and the megamaser sample of Läscher et al. (2016). L_{bulge} is found to have the tightest correlation with M_{BH} of the relationships examined here, and will provide the least biased M_{BH} estimates from photometry.
2. The $M_{\text{BH}}-L_{\text{galaxy}}$ relationship for active galaxies is only slightly less well defined than the $M_{\text{BH}}-L_{\text{bulge}}$ relationship, but when combined with the megamaser and quiescent galaxy samples, the scatter increases significantly. Large photometric surveys may forego bulge–disk decompositions and estimate unbiased black hole masses more quickly with total galaxy luminosity, ignoring galaxy morphology, but with a loss of accuracy.

3. The $M_{\text{BH}}-M_{\text{bulge}}$ relationship for active galaxies is linear, while the quiescent galaxy sample displays a steeper slope. Both samples agree at the low-mass end, and the agreement is better when the M/L prescriptions of Bell & de Jong (2001) are used rather than those of Into & Portinari (2013). The best-fit relationship for the combined active, megamaser, and quiescent samples agrees well with the relationship for the active galaxies alone, which also agrees well with the expectations from the high-resolution Illustris hydrodynamical simulations. Agreement with other simulations is less clear because of incompleteness at $M_{\text{BH}} \lesssim 5 \times 10^7 M_{\odot}$.
4. The active galaxy $M_{\text{BH}}-M_{\text{stars}}$ relationship tends to lie slightly below that of the quiescent galaxy sample, but there is excellent agreement with the best fit for the combined active, quiescent, and megamaser samples. There is also excellent agreement between the best-fit $M_{\text{BH}}-M_{\text{stars}}$ relationship for the active galaxies and the expectations from the high-resolution Illustris hydrodynamical simulations, but incompleteness affects comparisons with other simulations. Large photometric surveys with multiple filters will achieve better accuracy in predicted black hole masses using the stellar mass of the galaxy (based on a two-filter color) than the galaxy luminosity in a single filter.
5. The fraction of the black hole mass to the galaxy stellar mass is a strong function of black hole mass (but not stellar mass), with more massive black holes occupying larger fractions of $M_{\text{BH}}/M_{\text{stars}}$. The same trend is seen in the quiescent galaxy and megamaser samples, and the median black hole mass fractions at fixed black hole mass are similar between all three samples. The median value of the black hole mass fraction ranges from $\sim 0.01\%$ at $10^6 M_{\odot}$ to $\sim 1.0\%$ at $10^{10} M_{\odot}$ and follows the form $M_{\text{BH}}/M_{\text{stars}} \propto M_{\text{BH}}^{0.71 \pm 0.04}$. Studies that seek to compare different galaxy samples should be careful to account for this effect if the samples are not matched in black hole mass.

Dedicated to Marla: you were instrumental in helping a young girl to find her voice and not to be afraid of using it. You will be sadly missed.

We thank the anonymous referee for helpful suggestions that improved the content and presentation of this paper. We also thank Rachel Kuzio de Naray, Monica Valluri, and Vardha Bennert for helpful comments. M.C.B. gratefully acknowledges support from the National Science Foundation through CAREER grant AST-1253702, and through grants *HST* GO-11661 and *HST* GO-13816 from the Space Telescope Science Institute, which is operated by the Association of Universities for Research in Astronomy, Inc., under NASA contract NAS5-26555. Based in part on observations at Kitt Peak National Observatory, National Optical Astronomy Observatory (NOAO Prop. ID: 2011B-0120; PI: Bentz; NOAO Prop. ID: 2013A-0438; PI: Manne-Nicholas), which is operated by the Association of Universities for Research in Astronomy (AURA) under a cooperative agreement with the National Science Foundation. This publication makes use of data products from the Two Micron All Sky Survey, which is a joint project of the University of Massachusetts and the Infrared Processing and Analysis Center/California Institute of Technology, funded by the National Aeronautics and Space Administration and the National Science Foundation.

Facilities: *HST* (ACS, WFPC2, NICMOS), WIYN.

ORCID iDs

Misty C. Bentz  <https://orcid.org/0000-0002-2816-5398>

References

- Anglés-Alcázar, D., Faucher-Giguère, C.-A., Quataert, E., et al. 2017, *MNRAS*, **472**, L109
- Batiste, M., Bentz, M. C., Manne-Nicholas, E. R., Onken, C. A., & Bershad, M. A. 2017, *ApJ*, **835**, 271
- Bell, E. F., & de Jong, R. S. 2001, *ApJ*, **550**, 212
- Bell, E. F., McIntosh, D. H., Katz, N., & Weinberg, M. D. 2003, *ApJS*, **149**, 289
- Bentz, M. C., Denney, K. D., Grier, C. J., et al. 2013, *ApJ*, **767**, 149
- Bentz, M. C., & Katz, S. 2015, *PASP*, **127**, 67
- Bentz, M. C., Peterson, B. M., Netzer, H., Pogge, R. W., & Vestergaard, M. 2009a, *ApJ*, **697**, 160
- Bentz, M. C., Peterson, B. M., Pogge, R. W., & Vestergaard, M. 2009b, *ApJL*, **694**, L166
- Blandford, R. D., & McKee, C. F. 1982, *ApJ*, **255**, 419
- Bonoli, S., Marulli, F., Springel, V., et al. 2009, *MNRAS*, **396**, 423
- Cox, A. N. 2000, *Allen's Astrophysical Quantities* (4th ed.; New York: Springer)
- Degraf, C., Di Matteo, T., & Springel, V. 2011, *MNRAS*, **413**, 1383
- DeGraf, C., Di Matteo, T., Treu, T., et al. 2015, *MNRAS*, **454**, 913
- de Vaucouleurs, G. 1948, *AnAp*, **11**, 247
- Dubois, Y., Volonteri, M., Silk, J., et al. 2015, *MNRAS*, **452**, 1502
- Ferrarese, L., & Merritt, D. 2000, *ApJL*, **539**, L9
- Gallazzi, A., Brinchmann, J., Charlot, S., & White, S. D. M. 2008, *MNRAS*, **383**, 1439
- Gebhardt, K., Bender, R., Bower, G., et al. 2000, *ApJL*, **539**, L13
- Grier, C. J., Martini, P., Watson, L. C., et al. 2013, *ApJ*, **773**, 90
- Grier, C. J., Pancoast, A., Barth, A. J., et al. 2017, *ApJ*, **849**, 146
- Gültekin, K., Richstone, D. O., Gebhardt, K., et al. 2009, *ApJ*, **698**, 198
- Hamilton, T. S. 2014, AAS Meeting, 223, 145.02
- Häring, N., & Rix, H.-W. 2004, *ApJL*, **604**, L89
- Heckman, T. M., & Best, P. N. 2014, *ARA&A*, **52**, 589
- Herrmann, K. A., Hunter, D. A., Zhang, H.-X., & Elmegreen, B. G. 2016, *AJ*, **152**, 177
- Hopkins, P. F., Bundy, K., Croton, D., et al. 2010, *ApJ*, **715**, 202
- Into, T., & Portinari, L. 2013, *MNRAS*, **430**, 2715
- Jarrett, T. H. 2000, *PASP*, **112**, 1008
- Jarrett, T. H., Chester, T., Cutri, R., et al. 2000, *AJ*, **119**, 2498
- Kaviraj, S., Schawinski, K., Silk, J., & Shabala, S. S. 2011, *MNRAS*, **415**, 3798
- Kelly, B. C. 2007, *ApJ*, **665**, 1489
- Kelly, B. C., & Merloni, A. 2012, *AdAst*, **2012**, 970858
- Kim, J.-h., Wise, J. H., Alvarez, M. A., & Abel, T. 2011, *ApJ*, **738**, 54
- Kinney, A. L., Calzetti, D., Bohlin, R. C., et al. 1996, *ApJ*, **467**, 38
- Kormendy, J., & Ho, L. C. 2013, *ARA&A*, **51**, 511
- Kormendy, J., & Kennicutt, R. C., Jr. 2004, *ARA&A*, **42**, 603
- Kormendy, J., & Richstone, D. 1995, *ARA&A*, **33**, 581
- Krist, J. 1993, in ASP Conf. Ser. 52, *Astronomical Data Analysis Software and Systems II* (San Francisco, CA: ASP), 536
- Lapi, A., Raimundo, S., Aversa, R., et al. 2014, *ApJ*, **782**, 69
- Läsker, R., Ferrarese, L., & van de Ven, G. 2014, *ApJ*, **780**, 69
- Läsker, R., Greene, J. E., Seth, A., et al. 2016, *ApJ*, **825**, 3
- Lippai, Z., Frei, Z., & Haiman, Z. 2009, *ApJ*, **701**, 360
- Magorrian, J., Tremaine, S., Richstone, D., et al. 1998, *AJ*, **115**, 2285
- Marconi, A., & Hunt, L. K. 2003, *ApJL*, **589**, L21
- Mathur, S., Fields, D., Peterson, B. M., & Grupe, D. 2012, *ApJ*, **754**, 146
- McAlpine, S., Bower, R. G., Harrison, C. M., et al. 2017, *MNRAS*, **468**, 3395
- Meert, A., Vikram, V., & Bernardi, M. 2015, *MNRAS*, **446**, 3943
- Miller, L., Percival, W. J., Croom, S. M., & Babić, A. 2006, *A&A*, **459**, 43
- Mutlu-Pakdil, B., Seigar, M. S., Hewitt, I. B., et al. 2018, *MNRAS*, **474**, 2594
- Oogi, T., Enoki, M., Ishiyama, T., et al. 2016, *MNRAS*, **456**, L30
- Osterbrock, D. E., & Pogge, R. W. 1985, *ApJ*, **297**, 166
- Ostriker, J. P., Choi, E., Ciotti, L., Novak, G. S., & Proga, D. 2010, *ApJ*, **722**, 642
- Pancoast, A., Brewer, B. J., Treu, T., et al. 2014, *ApJ*, **445**, 3073
- Peng, C. Y., Ho, L. C., Impey, C. D., & Rix, H. 2002, *AJ*, **124**, 266
- Peng, C. Y., Ho, L. C., Impey, C. D., & Rix, H.-W. 2010, *AJ*, **139**, 2097
- Peterson, B. M. 1993, *PASP*, **105**, 247
- Peterson, B. M., Ferrarese, L., Gilbert, K. M., et al. 2004, *ApJ*, **613**, 682
- Reines, A. E., & Volonteri, M. 2015, *ApJ*, **813**, 82
- Schaye, J., Crain, R. A., Bower, R. G., et al. 2015, *MNRAS*, **446**, 521
- Schlafly, E. F., & Finkbeiner, D. P. 2011, *ApJ*, **737**, 103
- Schlegel, D. J., Finkbeiner, D. P., & Davis, M. 1998, *ApJ*, **500**, 525
- Sérsic, J. L. 1968, *Atlas de Galaxias Australes* (Cordoba: Observatorio Astronomico)
- Shabala, S. S., Kaviraj, S., & Silk, J. 2011, *MNRAS*, **413**, 2815
- Shankar, F., Bernardi, M., Sheth, R. K., et al. 2016, *MNRAS*, **460**, 3119
- Shirakata, H., Kawaguchi, T., Okamoto, T., et al. 2016, *MNRAS*, **461**, 4389
- Sijacki, D., Vogelsberger, M., Genel, S., et al. 2015, *MNRAS*, **452**, 575
- Skrutskie, M. F., Cutri, R. M., Stiening, R., et al. 2006, *AJ*, **131**, 1163
- Steinborn, L. K., Dolag, K., Hirschmann, M., Prieto, M. A., & Remus, R.-S. 2015, *MNRAS*, **448**, 1504
- Tonry, J. L., Dressler, A., Blakeslee, J. P., et al. 2001, *ApJ*, **546**, 681
- Trakhtenbrot, B., & Netzer, H. 2010, *MNRAS*, **406**, L35
- Trebtsch, M., Volonteri, M., Dubois, Y., & Madau, P. 2018, *MNRAS*, **478**, 5620
- Tully, R. B., Rizzi, L., Shaya, E. J., et al. 2009, *AJ*, **138**, 323
- Tully, R. B., Shaya, E. J., Karachentsev, I. D., et al. 2008, *ApJ*, **676**, 184
- van Dokkum, P. G. 2001, *PASP*, **113**, 1420
- Veilleux, S., Kim, D.-C., Rupke, D. S. N., et al. 2009, *ApJ*, **701**, 587
- Vogelsberger, M., Genel, S., Springel, V., et al. 2014, *MNRAS*, **444**, 1518
- Volonteri, M., Dubois, P., Pichon, C., & Devriendt, J. 2016, *MNRAS*, **460**, 2979
- Volonteri, M., & Natarajan, P. 2009, *MNRAS*, **400**, 1911
- Wandel, A. 2002, *ApJ*, **565**, 762
- Worthey, G. 1994, *ApJS*, **95**, 107
- Zibetti, S., Charlot, S., & Rix, H.-W. 2009, *MNRAS*, **400**, 1181